

Banner appropriate to article type will appear here in typeset article

Hierarchical parcel-swapping representation of turbulent mixing. Part 4. Extension to the viscous range and to mixing of scalars with nonunity Schmidt numbers

Masoomeh Behrang¹, Tommy Starick², Isaac Wheeler¹, Heiko Schmidt², Alan R. Kerstein³, and David. O. Lignell^{1†}

¹350 CB, Brigham Young University, Provo, UT 84602, USA

²Brandenburg University of Technology Cottbus-Senftenberg, Germany

³Consultant, 72 Lomitas Road, Danville, CA 94526, USA

(Received xx; revised xx; accepted xx)

Hierarchical Parcel Swapping (HiPS) is a multiscale stochastic model of turbulent mixing based on a binary tree. Length scales decrease geometrically with increasing tree level, and corresponding time scales follow inertial range scaling. Turbulent eddies are represented by swapping subtrees. Lowest-level swaps change fluid parcel pairings, with new pairings instantly mixed. This formulation suitable for unity Schmidt number Sc , is extended to nonunity Sc . For high Sc , the tree is extended to the Batchelor level, assigning the same time scale (governing the rate of swap occurrences) to the added levels as the time scale at the base of the $Sc = 3$ tree. For low Sc , a swap at the Obukhov-Corrsin level mixes all parcels within corresponding subtrees. Well-defined model analogs of turbulent diffusivity and mean scalar-variance production and dissipation rates are identified. Simulations idealizing stationary homogeneous turbulence with an imposed scalar gradient reproduce various statistical properties of viscous-range and inertial-range pair dispersion and of the scalar power spectrum in the inertial-advective, inertial-diffusive, and viscous-advective regimes. The viscous-range probability density functions of pair separation and scalar dissipation agree with applicable theory, including the stretched-exponential tail shape associated with viscous-range scalar intermittency. Previous observation of that tail shape for $Sc = 1$, heretofore not modeled or explained, is reproduced. Comparisons to direct numerical simulation allow evaluation of empirical coefficients, facilitating quantitative applications. Parcel-pair mixing is a common mixing treatment, e.g., in subgrid closures for coarse-grained flow simulation, so HiPS can improve model physics simply by smarter (yet nearly cost-free) selection of pairs to be mixed.

† Email address for correspondence: davidlignell@byu.edu

1. Introduction

Turbulent mixing processes are critically important in a wide range of applications. Given their ubiquitous presence, understanding and accurately modeling these processes is essential. However, this is challenging due to multiple time and length scales involved. The primary challenge in turbulent flow research is to develop models that capture the complexity of turbulent mixing processes with high fidelity while balancing computational efficiency.

Passive scalar mixing has been extensively studied experimentally and computationally; see, for example, reviews by Gotoh & Watanabe (2012), Warhaft (2000), and Shraiman & Siggia (2000). The mixing of passive scalars with varying Schmidt number is important for many problems, and accurate understanding and modeling of their transport is necessary in more complex systems that include nontrivial source terms, as in aerosol dynamics or reacting flows, such as combustion (Lignell *et al.* 2015).

Direct numerical simulation (DNS) provides highly detailed information on scalar structures and statistics, but at high computational cost with limitations on the Reynolds and scalar Schmidt numbers that can be considered simultaneously (Gotoh & Yeung 2013). A range of modeling approaches has been developed for both theoretical analysis and engineering application. Transport in homogeneous isotropic turbulence with a mean scalar gradient has been studied using several closure models for the scalar variance spectrum and other correlation functions. For example, Briard & Gomez (2017) studied spectrum scalings for a wide range of Prandtl (Schmidt) numbers using the eddy-damped quasi-normal Markovian (EDQNM) model. Bos (2014) studied scalar anisotropy statistics using the Lagrangian Markovianized field approximation (LMFA) closure model. And O’Gorman & Pullin (2005) modeled the velocity-scalar cospectrum to measure the mean scalar flux across scales using the sparse direct-interaction perturbation (SDIP) closure model, similar to the direct-interaction approximation (DIA) model of Kraichnan (1959). The linear-eddy model (LEM) of Kerstein (1991b), also developed by Kalda & Morozenko (2008), solves unsteady, one-dimensional scalar transport in a physical coordinate with isotropic turbulent advection modeled stochastically through measure-preserving triplet maps. LEM’s successor, one-dimensional turbulence (ODT), evolves momentum and scalar fields and can dynamically treat more general boundary-layer flows (Kerstein 2022).

Here, we study turbulent mixing of passive scalars with varying Schmidt number using the hierarchical parcel-swapping (HiPS) model (Kerstein 2013). HiPS as originally proposed is a minimal model of mixing in the inertial-range turbulent cascade. This formulation involves a binary tree structure in which length scales at successive tree levels decrease geometrically downward from the apex of the tree and corresponding time scales follow inertial-range scaling. Physical fluid parcels reside at the base of the tree, such that the tree structure serves only to prescribe the time advancement of the system state, involving advection and mixing sub-processes.

Turbulent advection is modeled by introducing randomly sampled eddy events, each of which swaps the positions of two equal-size subtrees. Each parcel has the same composition as its nearest neighbor, where there is only one nearest neighbor in the binary-tree geometry. When a swap causes a composition difference between nearest neighbors, the two parcels are fully and instantaneously mixed so as to restore equality of parcel compositions. Only a lowest-level swap,

in which each subtree is a single parcel, can rearrange parcel pairings and thus induce micromixing. On this basis, the model induces stepwise scalar length-scale breakdown leading ultimately to mixing at a prescribed dissipation scale, nominally the Kolmogorov microscale, thus broadly idealizing the phenomenology of passive diffusive scalars in inertial-range turbulence.

This formulation implies equivalence of the advective (Kolmogorov) and mixing-dominated (Batchelor) microscales η and η_b respectively, corresponding to unity nominal Schmidt number $Sc = \nu/D$, where ν is the kinematic viscosity and D is the molecular diffusivity. Model extension to nonunity Sc was additionally proposed (Kerstein 2013) but neither formulated in detail nor implemented.

Instead, applications to date have introduced a model variant in which the parcel state is the velocity vector \mathbf{v} , enabling flow-field simulation rather than adoption of a prescribed flow parameterization (Kerstein 2014, 2021). In principle, this approach can incorporate advected scalar fields, and the present study is in part intended to facilitate that future extension. The main goal, however, is to provide the first full description and demonstration of a treatment of scalar mixing, accommodating nonunity Sc , within the minimal flow-parameterization framework. In this context, the parcel state is simply the scalar value ϕ within the parcel and turbulent advection is effectuated by means of subtree swaps at rates based on the prescribed level-dependent time scales, avoiding any specification or use of an underlying velocity field.

For high Sc , this requires augmentation of the inertial scale range of the binary tree by appending levels at the bottom of the tree that represent the viscous-dissipation range. For this purpose, the added levels are all assigned the same time scale that applies to the bottom of the inertial range (nominally the Kolmogorov time scale). This corresponds to the physical picture of stepwise length-scale breakdown viscous-range scalar structure that is induced by the smallest available eddies, (the Kolmogorov eddies), until this process is balanced by molecular-diffusive smoothing at the Sc -dependent Batchelor scale. The consequent subtree swaps at scales well below the Kolmogorov scale, but attributed to Kolmogorov-scale eddies, constitute the model representation of distant interactions between flow scales and much smaller scalar structure that govern high- Sc phenomenology. For low Sc , the Obukhov-Corrsin scale η_{oc} is analogous to η_b , with $\eta_{oc} > \eta$, and accordingly, homogenization across subtrees corresponding to scale η_{oc} is enforced, albeit on the basis of Bernoulli trials rather than assured homogenization.

Application of swaps to marked fluid parcels, involving no scalar content or mixing thereof, is sufficient to time advance parcel-pair separations. The simplicity of this process allows analytical treatment and consequent deterministic advancement of the probability density function (PDF) of pair separation, complementing information gleaned from Monte-Carlo simulation. For both the inertial and dissipative regimes, it is shown that the results largely conform to known and theoretically predicted phenomenology.

Mixing phenomenology is investigated in a configuration that idealizes an imposed mean scalar gradient in statistically stationary homogeneous turbulence. Turbulent diffusivity and mean scalar-variance production and dissipation are shown to have precise mathematical meanings that allow them to be quantified straightforwardly in nondimensional form. HiPS simulations produce PDFs of scalar dissipation whose tail shapes conform to predictions of asymptotic analysis. Scalar power spectra are consistent with known scaling exponents governing the inertial-advective, inertial-diffusive, and viscous-advective ranges. Conversion

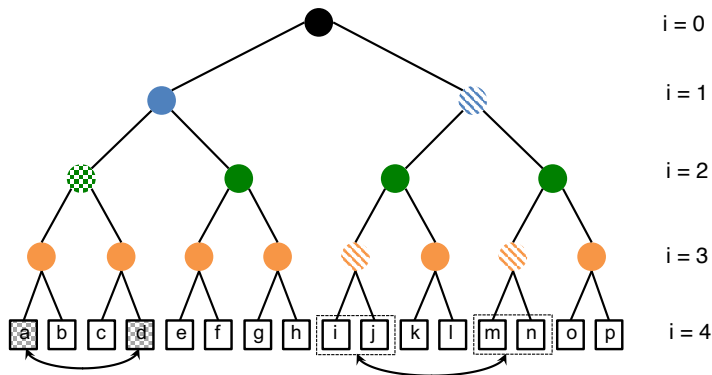


Figure 1: Schematic illustration of the binary HiPS tree showing nodes (circles) and fluid parcels (squares).

factors relating HiPS quantities to their physical counterparts are evaluated by comparing HiPS and direct numerical simulation (DNS) results. These conversion factors enable quantitative application of HiPS to turbulent mixing processes of interest. In this context, prospects for mixing/reaction closure of under-resolved three-dimensional turbulent flow simulations are discussed.

2. HiPS model

2.1. Model representation of flow advancement

HiPS is based on a binary tree structure. Each level of the tree is defined by a set of nodes. Each node branches into two sub-nodes, continuing to the bottom of the tree where fluid parcels reside. All fluid properties are defined only in the fluid parcels at the bottom of the tree, though mixing length and time scales are stored at the other node levels. In contrast to other hierarchical models, there are no filtered parcel states at other node levels.

Figure 1 illustrates the basic tree structure. The tree shown has $N_t = 5$ total levels. Nodes are indicated by circles and fluid parcels by squares. At the bottom of the tree, fluid parcels are paired as defined by their connecting node at the previous level. Tree levels are indexed beginning at zero at the tree apex.

Parcel proximity is defined as the level index of the nearest node connecting two parcels. In figure 1, parcel pairs (a, b) , (a, d) , (a, f) , and (a, p) have proximities at node levels 3, 2, 1, and 0, respectively. The proximity between a and either c or d is the same (at level 2); the proximity between a and any of e through h is the same (at level 1); and the proximity between a and any of i through p is the same (at level 0). The ordering of parcels with the same proximity is not relevant. For example, the tree state in figure 1 is unchanged if the first four parcels a, b, c, d were written as d, c, a, b , since the parcel proximities on the tree are the same.

Turbulent stirring is modeled by rearranging parcels. This involves a sequence of *eddy events*, each of which is implemented as follows:

(i) A given node of the tree is selected within accessible levels indexed $i = 0$ to $i = N_t - 3$; this is the base node.

(ii) A random node (or fluid parcel if $i = N_t - 3$) two levels down along the left branch emanating from the base node is randomly selected, and another node (or fluid parcel) is randomly selected two levels down along the right branch. These are grandchild nodes or parcels.

(iii) The two selected grandchildren of the base node are swapped (along with their subtrees in the case of swapping nodes).

Note that in step 2, grandchild nodes/parcels are selected two levels below the base node rather than selecting child nodes/parcels one level below the base node because the latter does not cause any change. The parcel proximity is what matters, not the left-to-right ordering suggested in figure 1.

Two swaps are shown in figure 1. The first is with the green checked base node at level 2. The two gray checked fluid parcels labeled a and d are randomly selected and swapped. This would change the pairing of parcels: $(a, b) \rightarrow (d, b)$ and $(c, d) \rightarrow (c, a)$. The second swap selects the blue striped base node at level 1. The two orange-striped grandchild nodes are randomly selected, and the two subtrees emanating from these nodes are swapped. In this case, those subtrees consist of fluid parcels i and j being swapped with parcels m and n . Note that in the second case, parcel pairings are not changed, whereas the parcel pairings are changed in the first case. That is, parcel pairings are only directly affected when swaps happen at the base node level indexed. Pairing of previously unpaired parcels is deemed to induce micromixing (implemented as explained in § 2.4), while mixing at other levels is macromixing that affects the spatial distribution of parcel states but not the internal compositions of individual fluid parcels. (This is true of unity Sc scalars. For arbitrary Sc , possibly with multiple scalars considered, micromixing may occur over more than two parcels. This is described in later sections.) The macromixing at levels $i < N_t - 3$ effectively *sweeps* the smaller scales while mostly inducing a stepwise breakdown of flow structure at the scale of the eddy event (base-node level), though it can also lead to backscattering, forming larger structures from smaller ones, consistent with the behavior of inertial-range turbulent eddies in real flows.

2.2. Tree length and time scales

Each tree level i is associated with a length scale, L_i , and a time scale, τ_i , with the largest scales, L_0 and τ_0 , at the apex of the tree. The length scale at each level is a factor $A < 1$ of that at the previous level, $L_{i+1} = L_i A$, which gives

$$L_i = L_0 A^i. \quad (2.1)$$

If we consider parcels to occupy fluid volume, then each subtree occupies half the volume as the tree above, with a length-scale ratio of A . As explained in Appendix A, the coordinate symmetry appropriate for a given application determines the associated A value, e.g. for spherical symmetry corresponding to a radial coordinate r such that volume scales as r^3 , $A = 2^{-1/3} \approx 0.8$, while for planar symmetry, $A = 1/2$ and parcel widths can be treated as uniform and L_0 scales as the number of parcels.

The largest eddy event at level $i = 0$ swaps half the parcels in each of the two tree halves. This corresponds to a largest eddy size $L_1 = L_0 A$, which is interpreted as the integral scale L_I .

We define two additional scales. The first, l^* , at level index i^* and with time

scale τ^* , corresponds to a scalar with unity Sc . This scale marks the transition between the inertial viscous regimes. It is analogous to the Kolmogorov scale η , and $l^* = C_\eta \eta$, where C_η is an empirical constant (see § 4).

The other scale is denoted l_s^* , and is at level i_s^* with time scale τ_s^* . It is analogous to the Batchelor scale, η_b , for $Sc > 1$, or the Obukhov-Corrsin scale, η_{oc} , for $Sc < 1$. The smallest eddy length scale on the tree has a level index of $N_t - 3$.

For convenience, we also define N^* as the number of levels corresponding to a unity Sc scalar. This gives $i^* = N^* - 3$. Scalars with $Sc > 1$ correspond to $l_s^* < l^*$, requiring additional tree levels and thus $N_t > N^*$.

The transition scale l^* can be written in terms of a HiPS Reynolds number,

$$l^* = L_0 Re^{-3/4}. \quad (2.2)$$

Using $l^* = L_0 A^{i^*} = L_0 A^{N^*-3}$ gives $Re = A^{-\frac{4}{3}(N^*-3)}$, relating Re and N^* .

The level time scales govern the frequency of eddy events, discussed in § 2.3, and are specified as follows. According to Kolmogorov's second similarity hypothesis (Pope 2000), the kinetic energy dissipation rate ϵ is constant in the inertial range ($i \leq i^*$). Based on $\epsilon \sim u^2/\tau \sim L^2/\tau^3$, constant ϵ implies $\tau \sim L^{2/3}$. Using $L_i = L_0 A^i$, this gives

$$\tau_{i \leq i^*} = \tau_0 \left(\frac{L_i}{L_0} \right)^{2/3} = \tau_0 A^{\frac{2}{3}i}. \quad (2.3)$$

The smallest eddies are nominally size η because smaller eddies are suppressed by viscosity. For scalars with low diffusivity, corresponding to $Sc > 1$, size- η eddies down-scale scalar-field structure through compressive-strain effects until the scalar structure is dissipated at scale η_b . The corresponding dissipation scale in HiPS is l_s^* , thus identifying the scale range $[l_s^*, l^*]$ as the HiPS analog of the viscous-advective range for $Sc > 1$.

The scalar phenomenology within this range is order-unity reduction of scalar spatial structure per Kolmogorov time scale. Notwithstanding the absence of physical eddies within this scale range, this stepwise scale reduction is emulated in HiPS by implementing swaps at all scales between l^* and l_s^* , where the time scale throughout this range is taken as $\tau_{i > i^*} = \tau_{i^*}$, giving

$$\tau_{i > i^*} = \tau_0 A^{\frac{2}{3}i^*}. \quad (2.4)$$

After each scale- l_s^* swap, mixing is implemented, marking the transition from the viscous-advective regime to the viscous-dissipative regime.

As mentioned in § 1, this models the distant interactions between the smallest physical eddies and scalar structure at smaller scales within the viscous-advective range. In addition to capturing high- Sc spatial structure, as shown in § 3, it gives a physically sound representation of Lagrangian histories, notably the Sc dependence of elapsed time for scale breakdown from η to η_b (Kerstein 1991a).

2.3. Eddy selection

The procedure for sampling eddy event times and eddy locations at levels and nodes is given in the following subsections.

2.3.1. Sampling of event times

An eddy rate λ_i is associated with each level. We expect, on average, one eddy in time τ_i at each node of a given level, so the rate at each node is $1/\tau_i$, and the

total rate of level- i events is

$$\lambda_i = \frac{2^i}{\tau_i}. \quad (2.5)$$

The total rate of all eddies Λ is the sum of the rates λ_i on each level.

Turbulent motions are in general correlated in space and time, resulting in local fluctuations of turbulence intensity that account for observed intermittency. For simplicity in HiPS, such correlations are ignored, so eddy occurrences are statistically independent and therefore constitute a Poisson process in time, devoid of any history effects (although in conjunction with the mixing process, the scalar field has highly consequential history dependence).

On this basis, the time increments Δt between successive eddy occurrences are sampled from an exponential distribution corresponding to a Poisson process with mean rate Λ ,

$$p(\Delta t) = \Lambda e^{-\Lambda \Delta t}. \quad (2.6)$$

Here, $p(\Delta t)$ is the PDF of spacing Δt between eddy events. The cumulative distribution function (CDF) is

$$P(\Delta t) = \int_0^{\Delta t} p(\Delta t') d\Delta t' = 1 - e^{-\Lambda \Delta t}. \quad (2.7)$$

Time increments between eddy occurrences are sampled from this CDF as

$$\Delta t = -\frac{\ln(U_r)}{\Lambda}, \quad (2.8)$$

where $U_r \in [0, 1]$ is a uniform random variate.

As explained below, all changes of the system state in the present HiPS implementation occur at the epochs of the instantaneous eddy events. Therefore the sequence of sampled time increments Δt fully specifies the temporal structure of the advancement. Algorithmically, a HiPS realization is a sequence of implementations of the state changes prescribed upon the occurrence of the successive eddy events. Strictly speaking, the Δt values are not needed to implement this sequence of state changes and could be generated during post-processing provided that the system state upon the completion of each event is saved. This illustrates that the notion of time advancement is a physical interpretation superimposed on the algorithmic implementation rather than being intrinsic to that implementation. For statistically stationary flow, single-time statistics are unaffected by time rescaling implemented by changing Λ , a model feature that has previously proven to be consequential (Kerstein 2014, 2021). The freedom to rescale time is invoked in § 3.2.4 to identify the adjustment of the time development of a transient flow that is needed to match its empirical rate of development.

2.3.2. Eddy level selection

The selection of the tree level of a sampled eddy event is described below. After a level is selected, the specific node at that level to which the eddy is attached is chosen with uniform probability from among the 2^i nodes at the level i .

The formulation is designed to capture the full scale range of scalar fluctuations, ranging from the integral scale to the smaller of l^* and l_s^* . The scale range for a given scalar depends on Sc . With multiple scalars of varying Sc , the tree will include levels sufficient to accommodate the scalar with the largest Sc .

For convenience here, the inertial range $l \geq l^*$ is labeled I , and the viscous range $l < l^*$ is labeled V . The eddy rates in the respective ranges are denoted Λ_I or Λ_V , and the total rate is $\Lambda = \Lambda_I + \Lambda_V$. To determine the region, a uniform random variate $U_r \in [0, 1]$ is selected; if $U_r \leq \Lambda_I/\Lambda$, region I is selected, otherwise region V is selected. We then select a particular level in the chosen region.

In the inertial range, the probability of an eddy event at level i is

$$p(i) = \frac{\lambda_i}{\Lambda_I}, \quad (2.9)$$

where $\Lambda_I = \sum_{i=0}^{i^*} \lambda_i$. Equations (2.3), (2.5) give λ_i , and consequently Λ_I , as

$$\lambda_i = \frac{2^i}{\tau_0 A^{2i/3}}, \quad (2.10)$$

$$\Lambda_I = \frac{1 - (2A^{-2/3})^{i^*+1}}{\tau_0(1 - 2A^{-2/3})}. \quad (2.11)$$

This provides the CDF as

$$P(i) = \sum_{j=0}^i \frac{\lambda_j}{\Lambda_I} = \frac{1 - (2A^{-2/3})^{i+1}}{1 - (2A^{-2/3})^{i^*+1}}. \quad (2.12)$$

Finally, i can be sampled as

$$i = \left\lceil \frac{\log_2(1 - U_r(1 - (2A^{-2/3})^{i^*+1}))}{1 - \frac{2}{3} \log_2 A} - 1 \right\rceil, \quad (2.13)$$

where U_r is a uniform random variate on $[0,1]$, (different from previous values).

In the viscous range, the probability of an eddy event at level i is

$$p(i) = \frac{\lambda_i}{\Lambda_V}, \quad (2.14)$$

where Λ_V is

$$\Lambda_V = \sum_{i=i^*+1}^{N_t-3} \lambda_i = \frac{1}{\tau^*} (2^{N_t-2} - 2^{i^*+1}). \quad (2.15)$$

The CDF is

$$P(i) = \frac{2^{i+1} - 2^{i^*+1}}{2^{N_t-2} - 2^{i^*+1}}, \quad (2.16)$$

from which i can be sampled, using a uniform random variate $U_r \in [0, 1]$, as

$$i = \left\lceil \log_2 \left(U_r(2^{N_t-2} - 2^{i^*+1}) + 2^{i^*+1} \right) - 1 \right\rceil. \quad (2.17)$$

2.4. Micromixing

Micromixing can be implemented either as an instantaneous event triggered by an eddy event or continuously in time. The former is employed here owing to its simplicity and efficiency.

l_s^* is the scale at which the HiPS analog of molecular diffusivity, as quantified in Appendix B, balances eddy diffusivity. This corresponds physically to diffusive spreading of the scalar across a level- i_s^* subtree over the time period corresponding

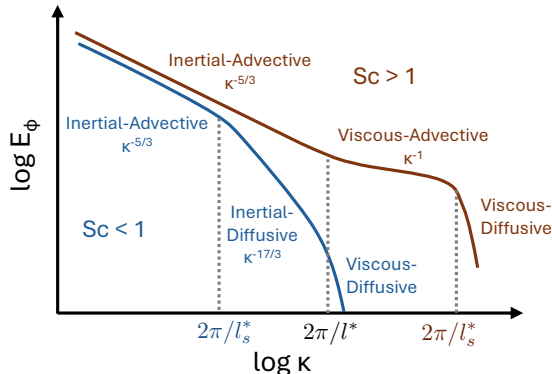


Figure 2: Schematic of the scalar variance spectra and regimes, where $\kappa = 2\pi/l$

to the mean time between eddy events at a given level- l_s^* base node. This balance is approximated as follows. After an eddy at a level- l_s^* base node is implemented, parcels in each of the two subtrees emanating from the base node are instantaneously mixed to the mean scalar value of the parcels in the given subtree. The scalar then has a uniform value in each of the two subtrees. A repetition of the same eddy and subsequent mixing can then impose uniformity across the two subtrees; but nonuniformity can be reintroduced by a subsequent level- $(l_s^* - 1)$ eddy that replaces one of the two subtrees below the base node.

For future applications, such as combustion, micromixing using mass-weighted (Favre) averaging of parcel properties may be desired.

2.5. Sc dependence

2.5.1. *Mixing phenomenology*

The Schmidt number is defined as usual, namely $Sc = \nu/D$, where ν and D are viscosity and diffusivity, respectively. The representation and quantification of these two fluid properties in HiPS are explained in Appendix B.

To orient the model description in terms of the mechanisms governing scalar mixing in turbulence, the standard phenomenology of mixing regimes is summarized in a schematic in figure 2 of the scalar variance spectra. The small-scale cutoff of the inertial range is denoted l^* rather than η because η is dimensionally prescribed and governs the parameter dependence of l^* but the physical cutoff differs from η by a numerical factor. For given Sc , there is a unique ratio l_s^*/l^* such that scale breakdown of scalar structure by fluid motion dominates the smoothing effect of molecular diffusion at scales $l > l_s^*$ but molecular diffusion inhibits such scale breakdown for $l < l_s^*$.

For $Sc > 1$, $l_s^* < l^*$, and for $Sc < 1$, $l_s^* > l^*$. For given Sc , there are three possible regimes depending on the magnitude of l relative to both l^* and l_s^* . The regimes are indicated in figure 2 where the first word refers to the flow regime and the second refers to the dominant influence at scale l .

The two Sc subranges differ qualitatively only in the phenomenology of the intermediate of the three regimes, and those regimes are particularly subtle in terms of both physics and modeling. For all regimes, the basic scaling properties

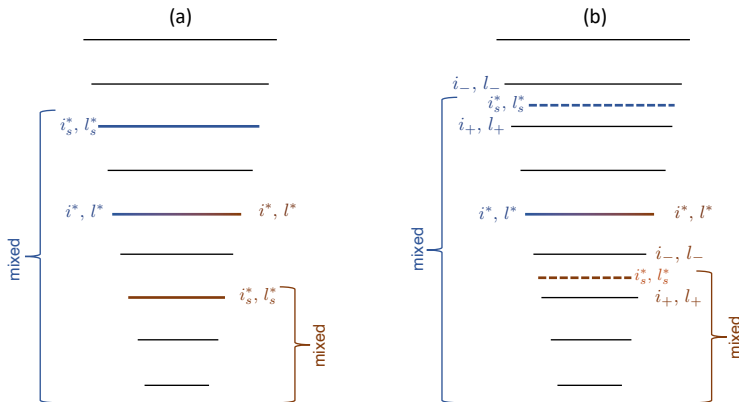


Figure 3: Schematic of HiPS tree levels; (a) for Sc corresponding to tree levels; (b) for Sc corresponding to scales between tree levels. In (a) and (b), the labels on the left side correspond to $Sc < 1$, those on the right correspond to $Sc > 1$.

are well established, including the Sc dependence of l_s^*/l^* . Those scaling properties will be specified in what follows with reference to the relevant literature.

By analogy to η and η_b or η_{oc} , the scales l^* and l_s^* are related in terms of the Schmidt number as

$$l_s^* = l^* Sc^{-1/p_s}. \quad (2.18)$$

For $Sc \geq 1$, $p_s = 2$, and for $Sc \leq 1$, $p_s = 4/3$ (Yeung & Sreenivasan 2013).

Section 2.5.2 considers scalars with l_s^* corresponding to discrete HiPS levels. Generalization to arbitrary l_s^* is given in § 2.5.3.

2.5.2. Discretized Sc values

Figure 3a shows schematics of two scalars on a given tree. The horizontal lines correspond to tree levels, with the decreasing line length from top to bottom corresponding to the decreasing length scale. Two scalars are shown with $Sc < 1$ and $Sc > 1$ on the left and right of figure 3a, respectively. Each scalar is mixed across the respective left and right subtrees emanating from nodes at level i_s^* , indicated by the brackets labeled “mixed” spanning levels $i > i_s^*$.

Equations (2.1), (2.18) combine to give the Schmidt number corresponding to scalars that mix at tree levels i_s^* relative to i_* ,

$$Sc = A^{-p_s(i_s^* - i_*)} = A^{-p_s \Delta i}. \quad (2.19)$$

For $A = 1/2$, and $p_s = 4/3$ for $Sc \leq 1$, we have $Sc \approx 1, 0.4, 0.16, 0.062, 0.025$, for $\Delta i = 0, -1, -2, -3, -4$, respectively. For $Sc \geq 1$, $p_s = 2$, $Sc = 1, 4, 16, 64, 256$, for $\Delta i = 0, 1, 2, 3, 4$, respectively.

2.5.3. Arbitrary Sc

Arbitrary Sc corresponds to scalars with l_s^* between two HiPS tree levels such that i_s^* may not be an integer. For a scalar with a given Sc , $\Delta i = -\log Sc / (p_s \log A)$,

or

$$Sc < 1 : \quad i_s^* = i^* - \frac{3 \log Sc}{4 \log A}, \quad (2.20)$$

$$Sc > 1 : \quad i_s^* = i^* - \frac{\log Sc}{2 \log A}. \quad (2.21)$$

Indices i_- and i_+ designate the lower and upper tree levels bounding i_s^* (see figure 3b). Eddy events that correspond to level indices at or greater than i_+ induce homogenization of the scalar throughout each of the left and right subtrees emanating from the level i_+ eddy node. For a level i_- eddy event, the scalar is mixed across the two subtrees of the level i_- node with probability p_- , where

$$p_- = \frac{i_+ - i_s^*}{i_+ - i_-} = i_+ - i_s^* = i_- - i_s^* + 1. \quad (2.22)$$

The second and third equalities hold since $i_+ - i_-$ is always unity. This probability is linear in index space and takes a value of 1 when $i_s^* = i_-$ and a value of 0 when $i_s^* = i_+$. Using (2.1), (2.3), and (2.5), p_- can be written as

$$p_- = \frac{\log(l_s^*/l_+)}{\log(l_-/l_+)} = \frac{\log(\lambda_s^*/\lambda_+)}{\log(\lambda_-/\lambda_+)}. \quad (2.23)$$

This illustrates that the linear interpolation in index space corresponds to logarithmic interpolation between eddy lengths, times or rates, consistent with the geometric progression of scales with tree level.

2.6. Map-based advection

A distinctive feature of HiPS is its implementation of advection as a sequence of instantaneous rearrangements of fluid parcels. In this sense a swap event is a type of map-based advection. Kerstein (2013) compares HiPS to other models involving advection treatments of this type. Unlike HiPS, those other models are time advanced in physical space, along a one-dimensional coordinate. It will be shown that HiPS can be formulated so that it likewise emulates flow evolution along a representative line of sight through a turbulent flow.

A swap of a pair of equal-size intervals can be performed on a 1D coordinate but this introduces property discontinuities that correspond to instantaneous nonlocal transfer of property fluctuations to wavenumber $\kappa = \infty$. To avoid this anomaly, a different map, termed the triplet map, is adopted (Kerstein 1991b).

The closest antecedent to the present HiPS formulation is the linear-eddy model (LEM) (Kerstein 1991b), in which the analogs of level-dependent HiPS length and time scales are a continuous range of map sizes and associated time scales that govern the time sequence of map occurrences. Between successive map occurrences, molecular transport of scalar properties is time advanced, so the microphysics is continuous in time rather than event-based.

In both HiPS and LEM, velocity fields have been introduced. They do not advect fluid directly, but instead they enable on-the-fly evaluation of map-size-dependent time scales that govern the sequence of map occurrences. These augmented formulations are denoted as flow HiPS (versus the present mixing HiPS) (Kerstein 2014) and one-dimensional turbulence (ODT) (Kerstein 2022) respectively. In flow HiPS, each subtree has an individually evaluated time scale that varies as the system state evolves. The present HiPS formulation will reach

its broadest range of applicability when its mixing phenomenology, encompassing all mixing regimes as parameterized by Sc , is incorporated into flow HiPS.

Flow HiPS is more comprehensively predictive than mixing HiPS in that level time scales are not preset (and vary from node to node within a given level as well as with time), and minimal empirical input is needed. Owing to the detailed validation of flow HiPS that has been performed (Kerstein 2014, 2021), the main focus here is on demonstration of the scalar advection-diffusion phenomenology that is captured by the present formulation.

3. Results

3.1. Simulated configurations

As formulated in the previous sections, HiPS simulations correspond to scalar mixing in homogeneous turbulence. In the following, we consider Lagrangian parcel-pair dispersion in homogeneous isotropic turbulence (HIT), as well as scalar mixing in HIT with a mean scalar gradient that is imposed using a jump-periodic boundary condition. This results in a statistically stationary scalar field as in DNS comparison cases. Pair-dispersion is discussed in the next section and the scalar-mixing results are discussed beginning in § 3.3.

For the scalar-mixing configuration, the scalar field is initialized to be uniform in each half of the tree, with a difference in value of $\Delta\phi_0$. The scalar gradient is then $\nabla\langle\phi\rangle = \Delta\phi_0/(L_0/2)$, giving a dimensionless scalar gradient of $G = 2$ when $\Delta\phi_0$ is taken as the reference scalar value and L_0 is the reference length scale.

Implementation of the jump-periodic boundary condition is analogous to its implementation in DNS. The intent in DNS is to obtain the equivalent of a row of DNS instantiations aligned with the mean scalar gradient, identical except that all scalar values in a given instantiation exceed their values in the down-gradient neighboring instantiation by $L_{\text{DNS}}\overline{\nabla\phi}$, where L_{DNS} is the domain length. The HiPS analog is to postulate a row of HiPS instantiations with the same properties. This is implemented through the treatment of the largest eddies that, in a closed domain, are level-0 swaps that move a quarter of the HiPS fluid volume from left to right, and a quarter from right to left, across the domain center. To enforce the mean scalar gradient, this level-0 swap is implemented with probability 1/2, the alternative (also with probability 1/2) being a level-0 swap analogous to DNS fluid crossing the boundary between adjacent instantiations. In the latter case, the quarter-tree that is swapped from right to left has its scalar values decreased by $2\Delta\phi_0$, while the values are increased by $2\Delta\phi_0$ in the other quarter-tree that moves from left to right. This is analogous to enforcement of the mean gradient in DNS by imposing a jump-periodic scalar boundary condition, although the HiPS implementation results in the scalar gradient being present only at the integral scale of the tree. Subtrees of any given half-tree have ensemble-mean scalar values equal to that of their parent half-tree. In § 3.4 it is shown that this formulation captures the leading-order phenomenology of scalar transport and mixing along a representative line of sight aligned with the imposed gradient.

3.2. HiPS dispersion

3.2.1. Background

The dispersion of a particle pair under the influence of turbulence is a fundamental problem in fluid dynamics (Elsinga *et al.* 2022). Dispersion refers here to the

separation time history of an initially close pair of particles. Predictions for turbulent dispersion of particle pairs date back to the publication by Richardson (1926) of an empirical approach indicating that the mean squared separation, $\langle Y^2 \rangle$, grows as the third power of time, t^3 , in inertial-range turbulence. Invoking Kolmogorov's similarity theory, Obukhov (1941) concluded that, for dispersion in the inertial subrange and after an initial induction time, $\langle Y^2 \rangle = g\epsilon t^3$, where g is the Richardson constant. This dispersion scaling follows dimensionally if the dispersion in the inertial range depends only on ϵ and time t .

3.2.2. Analysis of parcel-pair dispersion

Using the approach proposed in Kerstein (2013), the dispersion properties of HiPS are analysed by deriving a differential equation for the evolution of the probability of pair separation at given tree level. In HiPS, the separation r between two parcels of proximity i (defined above) is AL_i . For convenience, we refer to parcel separation index as the minimum number of levels k that need to be traversed to get from one parcel to another along a connected path within the HiPS tree. Then in figure 1, parcels a and b have separation $k = 1$, parcels a and d have separation $k = 2$, etc. Parcel separation index k is related to proximity index i as $k = N_t - 1 - i$, and separation r is related to k by $r = L_0 A^{N_t - k}$, giving increasing separation with increasing k . We consider separations $k \in \{1, 2, \dots, N_t - 1\}$.

Consider an ensemble of HiPS trees with n_p total parcel pairs across all trees that initially have separation index $k = 1$. Parcel separations must initially increase, but then eddy events can either increase or decrease the pair separation. The rate of change of the number of pairs with separation index k is given by

$$\frac{dn_k}{dt} = I_{k-1}n_{k-1} + D_{k+1}n_{k+1} - (I_k + D_k)n_k. \quad (3.1)$$

Here, I and D are the rates of eddy events that cause an increase I or a decrease D in parcel-pair separation. The subscripts on I and D indicate the separation *from which* the increase or decrease occurs. $I_{k-1}n_{k-1}$ is the rate of eddy events that increase the separation index from $k-1$ to k , times the number of pairs with separation index $k-1$, which gives the rate of change of the number of pairs with separation index k caused by increases from separation index $k-1$. The first two terms on the right-hand side of (3.1) create pairs with separation index k from neighboring index values (increase from $k-1$ or decrease from $k+1$). The third and fourth terms remove pairs of index k as they are increased or decreased to neighboring levels $k+1$ and $k-1$. Increases from $k-1$ to k occur by separation-level- k eddy events, and $I_{k-1} = 1/\tau_k$, where τ_k is the time scale at the tree level corresponding to separation index k . Similarly, decreases from $k+1$ to k occur by separation-level- $(k+1)$ eddy events, and $D_{k+1} = 1/(2\tau_{k+1})$. The $1/2$ factor on D is because half of such eddy events decrease the separation and half leave it unchanged, depending on the subtrees chosen for the swaps.

Dividing (3.1) by n_p gives the fraction of parcel pairs for separation index k , which corresponds to the probability P_k of separation index k . This constitutes a classic birth-death process, where the evolving separation of a given parcel pair is a continuous-time Markov chain (Crawford *et al.* 2018). Parcels with separation $k = 2$ correspond to level i^* . Then $\tau_k = \tau^*(L_k/l^*)^{2/3} = \tau^*A^{\frac{2}{3}(2-k)}$. Let $B = A^{2/3}$

and $T = t/\tau^*$; reordering terms, we can write (3.1) as

$$\frac{dP_k}{dT} = B^{k-2}P_{k-1} - \left(B^{k-1} + \frac{B^{k-2}}{2} \right) P_k + \frac{B^{k-1}}{2} P_{k+1}. \quad (3.2)$$

This is a system of coupled differential-difference equations with a tridiagonal matrix form. The initial condition is $P_1 = 1$, $P_{k>1} = 0$. The matrix of coefficients of P is singular since $\sum_k P_k = 1$, so we solve for $k = 1$ to $k = N_t - 2$, with $P_{N_t-1} = 1 - \sum_{k=1}^{N_t-2} P_k$. Note that for $k = 1$, the first and third additive terms in (3.2) are zero since there are no eddy events at the tree level corresponding to $k = 1$ ($i = N_t - 2$). Similarly, the second and fourth terms are zero for $k = N_t - 1$ since there are no levels above the apex of the tree. Equation (3.2) is solved analytically by an eigendecomposition.

The solution P_k with argument k can be converted into a physical-space pair-separation coordinate r based on conservation of probability, expressed as $P_k \Delta k = P(r) \Delta r$, where $\Delta k \equiv 1$. Using $\Delta r \approx (dr/dk) \Delta k$, with $r(k) = L_0 A^{N_t - k}$ gives $dr/dk = -r \ln A$, and $P(r) = -P_k/r \ln A$. Similarly, we can write $P(\ln r) = rP(r) = -P_k/\ln A$, emphasizing that $P(\ln r) \propto P_k$.

Beginning with the initial condition, the P_k profiles migrate to higher k in time. At large T , a stationary distribution is reached, which is given by

$$P_k = \frac{2^{k-1}}{\sum_{j=1}^{N_t-1} 2^{j-1}} = \frac{2^{k-1}}{(2_t^N - 2^{N_t-1} - 1)}. \quad (3.3)$$

This simply reflects that a given parcel's partner in the pair can have one position that has separation index $k = 1$, two positions with separation index $k = 2$, four positions with separation index $k = 3$, etc., consistent with the geometric growth of the number of parcels with tree level. After sufficient time, the partner location is statistically independent of the given parcel's location, resulting in stationarity.

The reasoning that yields the dependence $P_k \propto 2^k$ does not depend on details such as the k dependence of the coefficients of the terms in (3.2) so it is of particular interest to assess the physical meaning of this result. $P_k \propto 2^k$ implies

$$P(r) \propto 2^{-1 - \ln r / \ln A}, \quad (3.4)$$

which follows from $P(r) = -P_k/r \ln(A)$ and $r(k) = L_0 A^{N_t - k}$, given above. Stationarity requires $P(r) dr$ to scale as the d -dimensional volume element $r^{d-1} dr$, so $P(r) \propto r^{d-1}$. By counting of parcel pairs with level- k separation, (3.4) gives $A = 2^{-1/d}$, as explained in more detail in Appendix A. Thus, for consistency with the stationary solution for $P(r)$ in homogeneous isotropic turbulence, it is necessary to use $d = 3$ in the expression for A for the purpose of modeling parcel-pair dispersion.

The exact time advancement of HiPS pair dispersion according to (3.2) has the seemingly obvious property that the solution for the time advancement of P_k depends only on the initial value of P_k . In fact, this is not self-evident because many initial system states with nonequivalent multi-parcel correlation configurations might have the same distribution of pair separations. It is plausible that the evolution of these nonidentical systems could produce different P_k time histories. The exact result that this cannot happen in HiPS does not preclude the possibility that this happens during the time advancement of material particles in Navier-Stokes turbulence. A data comparison that addresses this issue is presented in § 3.2.5

3.2.3. Viscous-range dispersion

The current extension of HiPS to the viscous range allows investigation of viscous-range as well as inertial-range dispersion. Viscous-range dispersion phenomenology is of intrinsic interest as well as serving as a useful context for consideration of inertial-range dispersion.

Appendix C presents an analysis of the PDF of parcel-pair separation that approximates (3.2) by Taylor expanding the terms on the right-hand side. This reduces the set of differential-difference equations to (C2), a single partial differential equation. Specialization to the viscous range by setting B equal to unity, reflecting the uniformity of time scales across tree levels within the viscous range, yields a Fokker-Planck equation, (C3), reproduced here:

$$\frac{\partial P_k}{\partial T} = -V_d \frac{\partial P_k}{\partial k} + D_d \frac{\partial^2 P_k}{\partial k^2}, \quad (3.5)$$

where the two terms on the right-hand-side are drift and diffusion terms, respectively, and V_d and D_d are constants.

For a delta-function initial condition, (3.5) has a closed-form solution, (C4), that upon transformation from P_k to $P(r)$ yields (C5), reproduced here:

$$P(r) = \frac{1}{r(4\pi\hat{D}_dT)^{1/2}} \exp\left(\frac{[\ln(r/r_1) - \hat{V}_dT]^2}{4\hat{D}_dT}\right), \quad (3.6)$$

where $\hat{V}_d = V_d \ln(1/A)$, $\hat{D}_d = D_d [\ln(1/A)]^2$, and $r_1 = r(k=1)$.

Lognormality of the viscous-range pair-separation PDF is likewise obtained theoretically (Lundgren 1981) as well as from DNS (Girimaji & Pope 1990; Salazar & Collins 2009). As explained in Appendix C, the theory predicts numerical coefficients of the lognormal distribution that govern the relative strengths of the drift and diffusion terms. Owing to the A dependence that is introduced by transforming from argument k to argument $r \propto A^{-k}$ as in the derivation of (3.4), the corresponding coefficients in (3.6) depend on A . Exact agreement with the theoretical ratio of the two coefficients is obtained for $A = \exp(-2/9) \approx 0.8007$. The nearly exact agreement of this result with the symmetry requirement $A = 0.8$ (see Appendix A) is fortuitous in that the model thus embodies the necessary conditions for accurate representation of both the steady state and transient PDF shape evolution.

An initial-value problem on a finite domain cannot reproduce the lognormal distribution exactly. The consequent deviation from lognormality is demonstrated in figure 4a, which shows the time evolution of $P(\ln(r/r_1))$. This PDF is obtained by solving (3.2) for a tree with 50 levels with B set to unity for the initial condition $P_1 = 1$, $P_{k>1} = 0$, and Neumann conditions at the ends of the k range. In the plot coordinates, lognormality of $P(r)$ corresponds to a parabola. Although the deviations from lognormality are expected on a finite domain, they could also reflect approximations in the derivation of (3.5), but the good agreement seen for the times and r values least affected by the boundary conditions indicates that (3.5) closely approximates (3.2).

3.2.4. Inertial-range dispersion

Appendix C shows that Richardson similarity is imposed by construction in the inertial-range; this is explained heuristically in § 3.3. These considerations leave open the question of whether and how rapidly particle-pair statistics converge

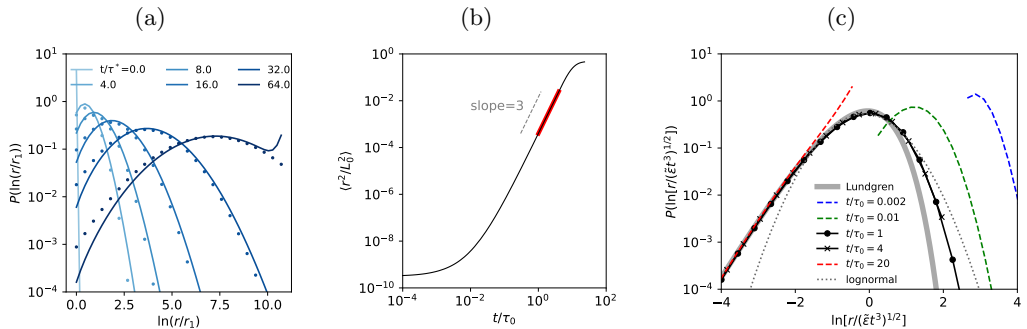


Figure 4: Pair-dispersion results for a tree with $N_t = 50$ levels and $A = 0.8$. (a) Pair-separation PDFs in the viscous regime at several times; lines are the solution of (3.2) with $B = 1$, symbols are (3.6). (b) Mean-square dispersion versus time in the inertial range. The red highlighted region indicates the similarity region reproducing Richardson's t^3 law. (c) Scaled pair-separation PDFs in the inertial range. Lundgren (1981) equation (5.26) is shown, along with a lognormal distribution. Dashed lines are PDFs at times earlier and later than the similarity regime. The $t/\tau_0 = 20$ PDF is the large- t stationary asymptote enforced by the bounded k range, corresponding to (3.3).

to the similarity scaling. Indeed, the mean-square separation is seen to converge to dependence on the cube of time, but this only becomes clear for a tree with about $N_t = 37$ levels, corresponding to $Re = 24,732$.

The need for a large scale range to obtain Richardson scaling is well known and its cause has been diagnosed (Elsinga *et al.* 2022). For HiPS, (3.2) circumvents the consequent high computational cost by enabling a direct exact solution for the pair-separation PDF evolution. Barring further theoretical progress, investigation of finer details such as first-passage times in the similarity regime would require Monte Carlo simulations. Symmetry considerations enable efficient numerical implementation, as explained in Appendix A.

The highlighted interval of the plot of $\langle r^2 \rangle$ demarcates the Richardson scaling regime that is examined further. For this purpose, HiPS pair-separation PDFs at selected times are plotted in figure 4c. For reference, a lognormal distribution is included with the same mean and variance as the $t/\tau_0 = 1$ curve. The two HiPS PDFs that collapse correspond to the times at the endpoints of the highlighted interval in figure 4b. HiPS PDFs at intermediate times within the highlighted interval (not shown) likewise coincide with the plotted HiPS PDFs. The self-similar form of the HiPS PDF is thus established.

Accordingly, the self-similar HiPS dispersion PDFs are compared in figure 4c to the inertial-range similarity solution

$$P(Y) = 37.0Y^2 \exp\{-3.52(Y^{2/3} + 0.165Y^{4/3})\} \quad (3.7)$$

derived theoretically by Lundgren (1981). Following the notations and conventions in that study, $Y \equiv r/(\tilde{\epsilon}t^3)^{1/2}$ with $\tilde{\epsilon} = C^{3/2}\epsilon$, and $C = 1.77$ is the Kolmogorov constant used by Lundgren. Since ϵ is indeterminate in HiPS, its HiPS value is evaluated by setting it relative to the theoretical ϵ so that the mode of the HiPS and Lundgren PDFs are equal in figure 4c. This enables evaluation of the Richardson constant g in the dimensional Richardson law $\langle r^2 \rangle = get^3$ based on the dependence shown in figure 4b. Proceeding first by treating nominal HiPS

time as physical time, $g = 4.68$ is obtained, which is 8.4 times higher than the value 0.56 that is obtained in recent studies (Elsinga *et al.* 2022). As explained in § 2.3.1, HiPS time advancement is invariant under time rescaling, allowing nominal HiPS time intervals to be adjusted in accordance with physical flow development. Then, to align the HiPS and physical g values, a given HiPS time interval is multiplied by $8.4^{1/3} = 2.0$ to obtain the corresponding physical time interval. This result is specific to $d = 3$, corresponding to $A = 0.8$.

Lundgren’s theory resembles other theoretical treatments of dispersion (Salazar & Collins 2009) in that it is based on Kolmogorov phenomenology and an eddy-diffusivity framework, but it is notable in its breadth of applicability beyond dispersion. Its case-specific depth of detail minimizes the required simplifications, but the detail tends to obscure the physics underlying the predicted trends. Comparison to HiPS results clarifies the governing physics.

This is shown by first revisiting viscous-range dispersion, governed by (3.2) with $B = 1$. For this choice of B , the k dependence of the coefficients on the right-hand side is eliminated, yielding a biased random walk that is invariant across scale space discretized into multiplicative strides. This yields lognormality of $P(r)$, as shown formally in Appendix C and inferred more heuristically (with DNS confirmation) by Girimaji & Pope (1990).

Taking this as the baseline for comparison to inertial-range dispersion, HiPS phenomenology straightforwardly explains the shorter tail of $P(r)$ in the latter regime. The swap operation is the same in both regimes albeit with different physical interpretations (representation of a physical eddy versus representation of the nonlocal effect of a Kolmogorov-scale eddy on a smaller-scale state). In either regime, a parcel pair is subject to separation by increasingly large swaps as pair separation increases. In the viscous range, swaps of all sizes occur at the same frequency, but in the inertial range, larger swaps are less frequent. Therefore, pairs that attain atypically large separation in the inertial range are subject to less rapid subsequent separation than if governed by viscous-range phenomenology. This implies a shorter-tailed inertial-range pair-separation PDF.

The format of figure 4c intentionally magnifies the difference between the HiPS and Lundgren PDFs in the tails. To the extent that the comparison indicates that Lundgren’s theory and HiPS embody much the same phenomenology, the main difference between them is that Lundgren invokes closure assumptions while (3.2) is an exact relation governing ensemble statistics of HiPS spatially and temporally resolved system advancement. The effect of closures is to suppress high-order correlations that are a salient cause of large deviations (Touchette 2009). Hence it is a reasonable hypothesis that HiPS embodies the fine-grained kinematics underlying dispersion phenomenology modeled on the basis of conventional Kolmogorov phenomenology and eddy diffusivity, allowing the further possibility that preservation of higher-order correlations in HiPS captures additional turbulence phenomenology beyond the Kolmogorov framework.

3.2.5. Multi-regime dispersion phenomenology

Figure 5 shows pair-separation PDFs for a case spanning the inertial and viscous ranges. An equation analogous to (3.2) is solved, but viscous-range phenomenology is introduced for k values less than a designated pair-separation level k^* corresponding to the transition between the inertial and viscous ranges. This is done by enforcing uniform time scales $\tau_k = \tau_{k^*}$ for separation levels $1 \leq k \leq k^*$.

Model results are compared to DNS results from Scatamacchia *et al.* (2012).

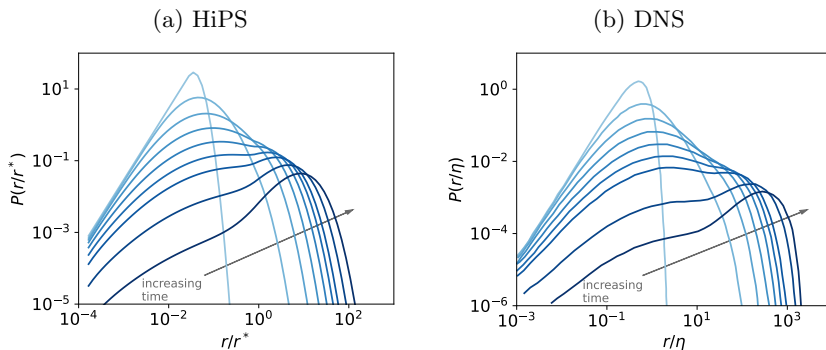


Figure 5: Dispersion PDFs: (a) HiPS, (b) DNS results from Scatamacchia *et al.* (2012). Times are at t/τ_η of 0, 10, 20, 30, 40, 50, 60, 80, and 110. The HiPS initial condition corresponds to $t/\tau_\eta = 10$ in Scatamacchia *et al.* (2012) (so their times are 10 units higher). Note the different axis scales used in the two plots owing to differing normalizations of r .

The initial condition is constructed to be qualitatively similar to that of Scatamacchia *et al.* (2012) by matching a linear profile to a parabolic profile (on log scales). The peak of the DNS initial PDF is close to $r/\eta = 1$. The relationship between η and k^* is not known *a-priori*. In principle it could be evaluated empirically using the procedure applied in §4, but to obtain a straightforward comparison of DNS and model PDF shape evolution, the initial HiPS profile is instead adjusted horizontally so as to obtain the best qualitative agreement between model and DNS results, which implicitly specifies the relationship between η and k^* . Then, for $N_t = 68$ levels and $k^* = 40$, the k location of linear-to-parabolic transition of the initial PDF profile, denoted k' , is set to 24.

Another consideration is the relationship between τ_η and its model analog τ^* , which affects both event frequencies and the specification of normalized data-collection times. We have taken the normalized model time t/τ^* to correspond to its physical counterpart t/τ_η . To proceed further we adopt the model calibration in § 3.2.4 establishing that HiPS time intervals must be multiplied by 2 to obtain the corresponding physical time intervals. The assumed equivalence of t/τ^* in terms of HiPS time and t/τ_η in terms of physical time therefore requires $2\tau^* = \tau_\eta$.

This calibration is needed for evaluation of the relationship between r^* and η . In HiPS, the starred variables are the characteristic dimensional quantities corresponding to the smallest scale of eddy occurrences. They are used to form an eddy-transport coefficient r^{*2}/τ^* that can be normalized by η^2/τ_η to define a Reynolds number Re_T that relates transition-scale eddy transport in HiPS to its nominal dimensionally defined analog. According to Kraichnan (1962), a suitable reference value for modeling purposes is $Re_T = 30$. Based on the definition of Re_T and the calibration $2\tau^* = \tau_\eta$, the relation $r^*/\eta = \sqrt{60} \approx 8$ is obtained. Thus, if the abscissa of figure 5a were converted from r/r^* to r/η , the numbers along the abscissa would increase by roughly an order of magnitude. Applying the same conversion to the argument of P , the Jacobian of the transformation would decrease the numbers along the ordinate of figure 5a by roughly an order of magnitude. These findings bring figure 5a into reasonable quantitative conformance with figure 5b.

On this basis, it is concluded that the chosen value of k' yields a suitable

facsimile of the DNS initial condition and that the main quantitative discrepancy of the HiPS results is excessively rapid falloff of the far tails of the PDFs that, owing to PDF normalization, slows the reduction of the peaks of the distributions.

These observations lend credence to the inputs to the parameter calibration, such as (3.7), and additionally to the analysis in Appendix C, which accordingly constitutes a plausible basis for interpretation of the results in figure 5. As noted, (3.6) governing the viscous range corresponds to drift and diffusion in terms of $\ln r$ with constant transport coefficients. For the more general setting in which the coefficients of the terms in (3.2) have any prescribed k dependencies, that equation embodies the same phenomenology except that the transport coefficients are now r dependent in a manner governed by the prescribed k dependencies.

On this basis, the phenomenology underlying the time development of the PDF shapes can be viewed in terms of the combined influences of drift and diffusion. The rapid depletion at small r and the emerging shoulder suggest ongoing drift of probability out of the viscous range that encounters a bottleneck in the inertial range where time scales progressively increase. Drift dominance is further indicated by the decrease in time of the small- r slope rather than increase toward the r^2 stationary solution that diffusion dominance would imply. At r values beyond the transitional bottleneck, drift-dominated evolution is likewise evident as indicated by the emergence of a large- r dome that seems to be approaching an invariant shape that slowly broadens as it drifts rightward.

Before these late-time features emerge, there is a brief transient appearance of a marginally bimodal shape. This transient is associated with bunching of the large- r PDF tails in the plot format, followed by greater separation of the successive tails as the dome shape emerges.

The foregoing observations apply equally to the HiPS and DNS results, reflecting the absence of any identifiable qualitative differences between them. Quantitative differences could be at least partly attributable to finite-Reynolds-number effects. In this regard, the Taylor-scale Reynolds number of the DNS case is 300. Although the HiPS k range is necessarily finite, inertial-range Kolmogorov phenomenology is embedded by means of the prescribed k dependencies of the coefficients of the terms in (C 2), which is a Taylor-expanded form of (3.2).

Scatamacchia *et al.* (2012) describe the apparent lognormality of PDFs in figure 5b at small r as a non-trivial result. Present results impart a precise meaning to this characterization. Pair-dispersion phenomenology has been shown here to be broadly encompassed by the drift-diffusion paradigm.

Finally, the agreement of figure 5a with figure 5b supports the implication of HiPS dispersion analysis, noted at the end of § 3.2.2, that a given initial pair-separation PDF uniquely determines the subsequent time evolution of the PDF for homogeneous isotropic turbulent flow, at least to a good approximation. To the authors' knowledge, evidentiary support for this proposal has not previously been reported.

3.3. *Turbulent flux and turbulent diffusivity*

Turning now from purely advective pair dispersion to the phenomenology of passive-scalar advection-diffusion, the model formulation is extended by introducing the scalar field ϕ that is subject to micromixing as described in § 2.4 and jump-periodic boundary conditions as described in § 3.1. Importantly, the underlying flow is still stationary homogeneous isotropic turbulence but the change in the desired outputs from Lagrangian pair-separation statistics to the structural

properties of the scalar field requires a fundamental change of perspective. As in previous related work (Kerstein 1991b), this is done by interpreting the HiPS domain as a line of sight aligned with the mean gradient. The phenomenological efficacy of the adopted approach is demonstrated by the exact analyses below, in § 3.4, and in Appendix D.

For reasons noted below (3.4) and in Appendices A and C, $A = 0.8$ is required for the model application to pair dispersion. For the model application to the imposed-scalar-gradient configuration, the choice $A = 1/2$ is implicit in the model formulation but there would be no identified inconsistency resulting from another choice (see Appendix A). $A = 1/2$ has been adopted in part owing to its suitability for intended future applications.

The turbulent diffusivity D_T is defined in relation to the turbulent scalar flux f using a Boussinesq assumption,

$$f = \langle \mathbf{u}' \phi' \rangle = -D_T \nabla \langle \phi \rangle, \quad (3.8)$$

where \mathbf{u}' is a velocity fluctuation (used for reference to standard treatments) and ϕ' is the scalar fluctuation referenced to the local mean.

The precise meaning of f for the present HiPS configuration follows from Gauss' theorem applied, for convenience, to scalar transfer to the right half-tree across the domain center. Only level-0 internal (vs. jump-periodic) swaps can perform such transfers. $\langle \phi \rangle$ is uniform within each half-tree, precluding any contribution of smaller-scale swaps to the mean flux whether defined globally or locally.

On average, one swap across the domain center changes the scalar value in half of the parcels in the right half-tree by the amount $-\Delta\phi_0$. Based on the half-tree size $L_0/2$, the corresponding mean scalar transfer during a time interval T is $-n\Delta\phi_0 L_0/4$, where the average number n of internal level-0 swaps during the time interval T is $T/(2\tau_0)$ because only half of the level-0 swaps are internal. The dimensionless flux is obtained by dividing by T and normalizing, giving

$$\frac{f}{L_0 \Delta\phi_0 / \tau_0} = -\frac{1}{8}. \quad (3.9)$$

For a three-level tree, this result is obtained in Appendix D by means of exhaustive enumeration of system states and the swap-induced transitions between them.

Using the convention $\nabla \langle \phi \rangle / (\Delta\phi_0 / L_0) \equiv G = 2$ in § 3.1, (3.8) and (3.9) give

$$\frac{D_T}{L_0^2 / \tau_0} = \frac{1}{16}. \quad (3.10)$$

Importantly, (3.10) can be obtained without invoking the flux-gradient relationship. Level-0 swaps induce a random walk of fluid parcels with diffusivity $D_T = L^2 / 2\tau$, where L is the parcel displacement for each event, and τ is the time between events. Evaluation of L and τ based on the considerations that have been described recovers (3.10). Random-walk analysis is the basis of the scalar-dissipation analysis in Appendix E and is implicit in the dispersion analysis in Appendix C, which does not involve a scalar field. In Appendix B, a random-walk approach is used to analyze the HiPS molecular diffusivity. These examples illustrate the breadth of applicability of the random-walk perspective relative to the flux-gradient relationship.

The random-walk perspective likewise extends to the level-dependent turbulent diffusivity of index- i swaps, yielding $D_i \propto l_i^2 / \tau_i$. For the inertial range, $\tau_i \propto l_i^{2/3}$

so $D_i \propto \tau_i^2$. Then in the notation of § 3.2.4, $d\langle r^2 \rangle / dt \propto D(r) \propto t^2$, yielding the Richardson scaling. Hence, this scaling is seen to follow directly from enforcement of $\tau_i \propto l_i^{2/3}$ in HiPS. A related explanation in terms of the HiPS dispersion formalism is provided in § 3.2.4.

3.4. Production and dissipation

In homogeneous turbulence, the scalar variance $\langle \phi'^2 \rangle$ is given by

$$\frac{\partial \langle \phi'^2 \rangle}{\partial t} = -2\langle \mathbf{u}'\phi' \rangle \cdot \nabla \langle \phi \rangle - 2D\langle \nabla \phi' \cdot \nabla \phi' \rangle = \mathcal{P} - \langle \chi \rangle. \quad (3.11)$$

The right-hand side of this equation gives the difference between the mean scalar-variance production

$$\mathcal{P} = -2\langle \mathbf{u}'\phi' \rangle \cdot \nabla \langle \phi \rangle \quad (3.12)$$

and the mean scalar-variance dissipation rate $\langle \chi \rangle$ (Yeung & Sreenivasan 2014).

HiPS does not have a continuous physical domain, so calculation of production and dissipation using the standard definitions cannot be done directly. However, mean production and dissipation can be evaluated based on their roles as a scalar-variance source and sink, respectively.

Using (3.12), the first equality in (3.8), (3.9), and $\nabla \langle \phi \rangle = 2\Delta\phi_0/L_0$, the nondimensional production

$$\frac{\mathcal{P}}{(\Delta\phi_0)^2/\tau_0} = \frac{1}{2} \quad (3.13)$$

is obtained. At steady state, production and dissipation balance and we have

$$\frac{\langle \chi \rangle}{(\Delta\phi_0)^2/\tau_0} = \frac{1}{2}. \quad (3.14)$$

These values were verified in HiPS simulation as follows. Production occurs due to level-0 eddies that transport fluid across the mean scalar gradient. In each half-tree, \mathcal{P} is computed as the running sum of the difference in scalar variance before and after level-0 eddy events, divided by the simulation time. The values in each half-tree are then averaged. Recall that level-0 eddy events do not change the scalar values of individual parcels. The mean dissipation is computed similarly. In each half-tree, the running sum of the difference in scalar variance before and after eddies resulting in micromixing is accumulated, and this sum is then divided by the simulation time. Finally, the average of the two half-tree results is computed.

These evaluations serve to illustrate the physical fidelity of the adopted line-of-sight representation of scalar-field evolution in the imposed-mean-gradient configuration. Equation (3.12) shows that production is fully captured by such a representation. The conservative model treatment of scalar-field evolution assures that dissipation equals production. Without multiple coordinate directions in which to dissipate scalar variance, local scalar gradients must be higher by an order-unity factor than in three-dimensional physical space. Model simplifications relative to Navier-Stokes phenomenology necessarily introduce errors of this magnitude, so this artifact does not materially degrade model performance. To some extent, the artifact is subsumed in the calibration of model parameters, as in § 4. Appendix D shows an exact calculation of the production and dissipation for a three-level tree, indicating how the described phenomenology is captured in a configuration of irreducible simplicity.

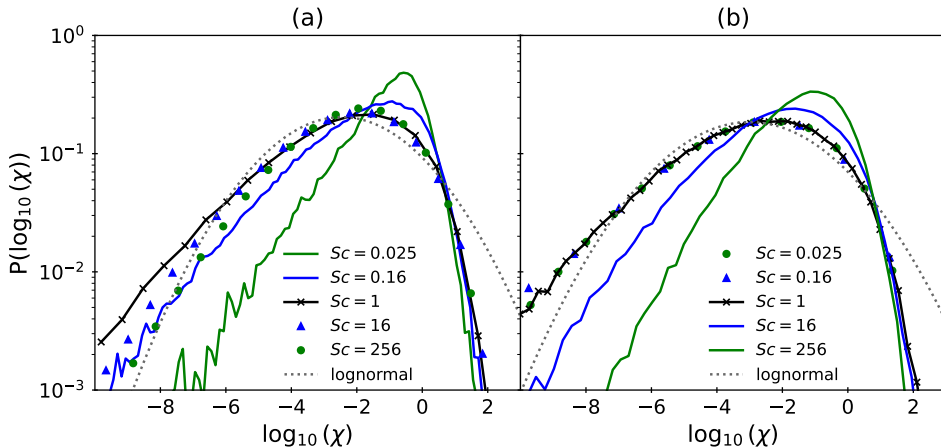


Figure 6: PDFs of $\log_{10}(\chi)$ for varying Sc for (a) constant Re , and (b) constant Sh . Symbols are used for clarity to indicate PDFs that collapse. For each plot, a lognormal distribution is shown with parameters corresponding to $Sc = 1$.

Analogous considerations have been discussed in the context of the LEM modeling framework (Kerstein 1991b). That approach simulates scalar-field evolution on a 1D domain that likewise represents a line of sight aligned with the mean scalar gradient. Both the present HiPS formulation and the previous LEM formulation are precise analogs of the imposed-mean-scalar-gradient configuration as studied extensively by means of DNS (Donzis *et al.* 2010; Gotoh & Watanabe 2012; Shete *et al.* 2022; Watanabe & Gotoh 2004; Yeung & Sreenivasan 2014), theoretical analysis (Chertkov *et al.* 1998; Lundgren 1981), and modeling, notably in the latter regard using the Eddy-Damped Quasi-Normal Markovian model (Briard & Gomez 2017) and the Lagrangian Markovianized Field Approximation (Bos 2014).

3.5. PDFs of scalar-variance dissipation rate

Unlike the evaluation of \mathcal{P} and $\langle\chi\rangle$, evaluation of the PDF of χ is not uniquely prescribed on a first-principles basis. We present two approaches for its computation. The first approach makes use of the standard definition of χ given above in (3.11). The gradient $\nabla\phi'$ is computed as $\Delta\phi/\min(l^*, l_s^*)$, where $\Delta\phi$ is the difference in scalar value between two neighboring parcel pairs. The diffusivity D is not considered directly, rather, χ is scaled so that $\langle\chi\rangle = \int \hat{\chi}P(\hat{\chi})d\hat{\chi}$, where $\langle\chi\rangle$ is evaluated as described above.

The second approach computes χ using the following scaling: $\chi = 2D\nabla\phi' \cdot \nabla\phi' \sim (\Delta\phi)^2/\tau$. Here, τ is a time scale between the micromixing events. In HiPS, we take τ to be the time since the last change of the parcel state due to micromixing events and denote this as τ_{tlc} . The $\Delta\phi$ is computed as $\tilde{\phi} - \hat{\phi}$, where $\tilde{\phi}$ and $\hat{\phi}$ are the scalar value of a given single parcel before and after an eddy event, respectively. $P(\chi)$ is then constructed, and we apply the same χ scaling as used in the first approach. It is found that these two approaches give nearly the same results.

Here we present the dissipation PDF using the second approach to compute χ and examine the impact of Re and Sc variations. PDFs of $\log_{10}(\chi)$ are shown in figure 6. Table 1 gives corresponding simulation parameters.

Table 1: Simulation parameters corresponding to figure 6.

Figure 6a, constant Re					Figure 6b, constant Sh				
Sc	Re	Sh	i^*	i_s^*	Sc	Re	Sh	i^*	i_s^*
0.0248	256	22.22	6	2	0.0248	65536	5689	12	8
0.1575	256	141.1	6	4	0.1575	10321	5689	10	8
1	256	896	6	6	1	1625	5689	8	8
16	256	14336	6	8	16	101.6	5689	5	7
256	256	229376	6	10	256	6.35	5689	2	6

Figure 6a shows results for five Sc ranging from 0.0248 to 256 at constant Re , corresponding to a tree with $i^* = 6$ and $N^* = 9$. The dissipation PDFs nominally collapse for $Sc \geq 1$ except in the low χ tail. For these cases at constant Re , the scalar time scale τ_s^* is constant. Figure 6b shows results for the same Sc values, but at constant Sherwood number, Sh , given by

$$Sh = \frac{D_T}{D} = \frac{(2 - A^2)ScRe}{8A^4}, \quad (3.15)$$

where (3.10), (B 2), $Re = A^{-\frac{4}{3}i^*}$, and $i^* = N^* - 3$ are used, and use of (B 2) restricts (3.15) to integer i_s^* . Note that $Sh \propto Pe \equiv ScRe$ in HiPS. The Sherwood number is the mass-transfer analog of the Nusselt number Nu and is preferred when considering multiple scalars with unequal diffusivities. For constant Sh , Figure 6b shows collapse of the dissipation PDFs for $Sc \leq 1$. For $Sc \leq 1$, i_s^* , and hence τ_s^* and l_s^* , are constant.

Analysis and modeling suggest lognormality of the dissipation rates of kinetic energy (Obukhov 1962; Kolmogorov 1962) as well as various scalar properties including the scalar variance (Gurvich & Yaglom 1967). The latter reference introduces a simple model of scalar dissipation involving a geometric hierarchy of levels but no representation of Sc effects. It is concluded that the breadth of the PDF should increase as the number of levels increases.

Such a trend is indicated in Figure 6 in terms of deviation from the lognormal shape rather than lognormality *per se*. In both plots, the extreme rightmost tails of the PDFs broaden with increasing i_s^* , yet with faster than lognormal falloff in all instances.

For $Sc = 1$, similar PDF shapes, including broader-than-lognormal low- χ tails, were reported by Kerstein (1991b) based on LEM simulations and by Su & Clemens (2003) based on measurements in planar jets. Juxtaposed with this is the DNS result (Shete *et al.* 2022) shown in Figure 7a. Consistent with the HiPS setup, the DNS case is homogeneous turbulence with a mean scalar gradient from Shete *et al.* (2022). The DNS has a Taylor Reynolds number of $Re_\lambda = 633$.

Re_λ for HiPS is evaluated using an analysis from Gotoh & Watanabe (2012). They develop a statistical theory for the scalar flux and show that $Nu \approx C_q Sc Re_\lambda^2$, where the Kolmogorov constant is the only empirical input needed to obtain $C_q = 0.734$. This expression is used in HiPS, replacing Nu with Sh . Using (3.15) gives

$$Re = \frac{8A^4}{2 - A^2} C_q Re_\lambda^2 \approx 0.21 Re_\lambda^2, \quad (3.16)$$

where the final result is for $A = 0.5$. This equation completes the specification of the relationships between the parameters of the HiPS and corresponding DNS cases.

A caveat regarding (3.16) is that the accuracy of the theoretical result for Nu is not firmly established. It is used as an interim procedure for relating Re to Re_λ . Sh values for DNS cases are generally not reported but they are readily extractable from outputs, so the best future procedure is to use HiPS Sh values equal to the DNS values.

On this basis, figure 7a shows the dissipation PDF for HiPS at $Re_\lambda = 559$ for a tree with $N^* = 15$ levels, along with the DNS PDF and a lognormal distribution for reference. The DNS PDF follows the lognormal distribution closely, except at high dissipation. The HiPS PDF falls off more gradually at low dissipation and more rapidly at high dissipation. Notwithstanding this quantitative discrepancy, the HiPS high-dissipation tail exhibits a phenomenologically significant functional form, as discussed in § 3.6.

Figure 6 is plotted in non-normalized coordinates in order to reflect the Re and Sc dependencies on low moments (mean and variance) of the PDFs. DNS studies generally show only normalized PDF with no separate reporting of the low moments. The novel capability of HiPS to predict these quantities motivates an ongoing effort to acquire the relevant data for comparison purposes, results of which will be reported elsewhere.

3.6. High-dissipation phenomenology

Holzer & Siggia (1994) studied passive scalar mixing in two dimensions and found good agreement with experimental data in more complex configurations. They show that a stretched-exponential function fits the dissipation PDF in the large-dissipation tail. Chertkov *et al.* (1998) analyzed high- Sc scalar advection using the Kraichnan (1974) model. They derived an expression for $P(\chi)$, which can be represented as $\log(P(\chi)\chi^{1/2}) \propto \chi^{1/3}$. For $\chi \gg \langle \chi \rangle$, the PDF is given by a stretched exponential, with $\log P(\chi) \propto \chi^{1/3}$.

Figure 7b shows $\log_{10}(P(\chi)\chi^{1/2})$ and $\log_{10}(P(\chi))$ versus $\chi^{1/3}$ for HiPS at $Re = 256$ and $Sc = 1$, $Sc = 256$. Note that the $Sc = 1$ curves have been vertically shifted for clarity. Linear fits through the 12 largest χ values are shown, corresponding to Chertkov's model in the coordinates plotted. It is seen that for both Schmidt numbers, the HiPS data reproduces the predicted 1/3 exponent. Moreover, the fit is better when the subdominant $\chi^{1/2}$ factor is included, indicating the possibility that the model captures this dependence.

The 1/3 exponent for $Sc = 1$ is unexplained beyond speculative proposals although it has prior empirical support (Chertkov *et al.* 1998). It is additionally supported by recent DNS results (Dotson, Yeung & Sreenivasan, unpublished).

Insofar as the Chertkov *et al.* (1998) analysis is applicable at least at high Sc , it embodies the distant interactions between Kolmogorov eddies and much smaller scalar structures in the viscous-advective regime. As explained in § 1, the HiPS representation of this regime likewise embodies that phenomenology, perhaps hinting at common features of the analysis and the model whose elucidation could clarify the significance of the 1/3 exponent. Apart from the specific exponent value, the broader question of the phenomenological origin of the stretched-exponent tail of the HiPS PDF is addressed in Appendix E.

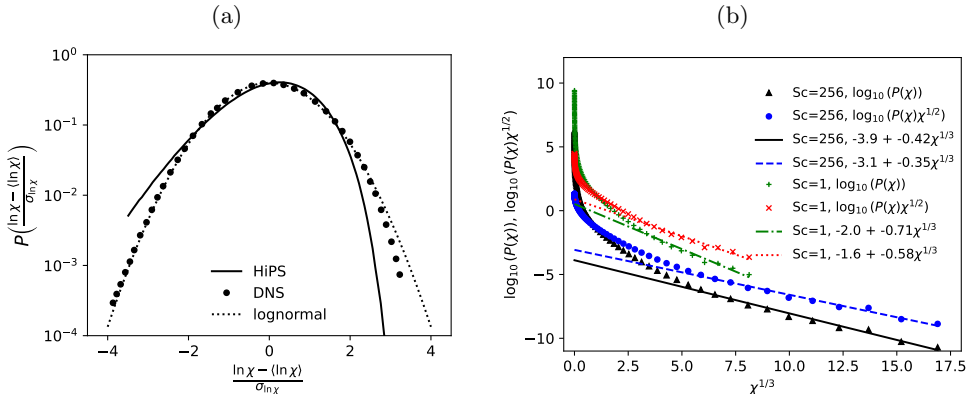


Figure 7: (a) Dissipation PDFs for $Sc = 1$ and $Re_\lambda = 559$ (HiPS); $Re_\lambda = 633$ (DNS of Shete *et al.* (2022)). (b) PDFs of scalar dissipation for $Re = 256$ and $Sc=1$, $Sc=256$ plotted on coordinates for comparison to Chertkov *et al.* (1998) for the scaling of the high χ tail. The $Sc=1$ curves are shifted by 2.5 vertical-axis units for clarity.

3.7. Scalar spectra

Scalar transport in turbulent flow is commonly represented and analyzed using the scalar variance spectrum. A detailed interpretation of the scalar variance spectrum in the context of HiPS was provided by Kerstein (2013) but no computations were performed. Here we provide a summary description and computations of the scalar spectrum for various Schmidt numbers.

In HiPS, the scalar variance spectra are inferred from the differences of scalar variances at adjacent levels of the tree. As noted by Kerstein (2013), the quantity $\int_\kappa^\infty E(\kappa') d\kappa'$ “scales as the variance of scalar fluctuations associated with wavenumbers exceeding κ ,” so to evaluate the integral and ultimately $E(\kappa)$, the wavenumber-restricted variance is first evaluated. The tree structure of HiPS has discrete, geometrically decreasing length scales with increasing tree level. We can think of each level i of the tree as having a corresponding wavenumber κ_i with $l_i = 2\pi/\kappa_i$. A discrete scalar spectrum is then given by

$$E(\kappa_i) = \frac{\text{var}_i \phi - \text{var}_{i+1} \phi}{\kappa_{i+1} - \kappa_i}. \quad (3.17)$$

As A approaches unity, this converges to the familiar continuum relationship between the scalar spectrum and the variance of the filtered scalar field, assuming spectrally sharp filtering.

Scalar spectra are obtained for three mixing regimes: inertial-advective, inertial-diffusive, and viscous-advective. Figure 8 shows scalar spectra from HiPS simulations over a range of Schmidt numbers.

The inertial-advective regime is characterized by turbulent scalar transport with negligible diffusive effects and spectral transfer from large to small scales is governed by the scalar-variance dissipation rate χ , which is independent of the length scale. The increasing advective rate with decreasing length results in quasi-stationary behavior that responds quickly to scalar variance transferred from larger scales. In this regime, time scales are related to length scales as $\tau \sim l^{2/3}$ and the kinetic-energy spectrum exhibits $\kappa^{-5/3}$ scaling. In HiPS, this time

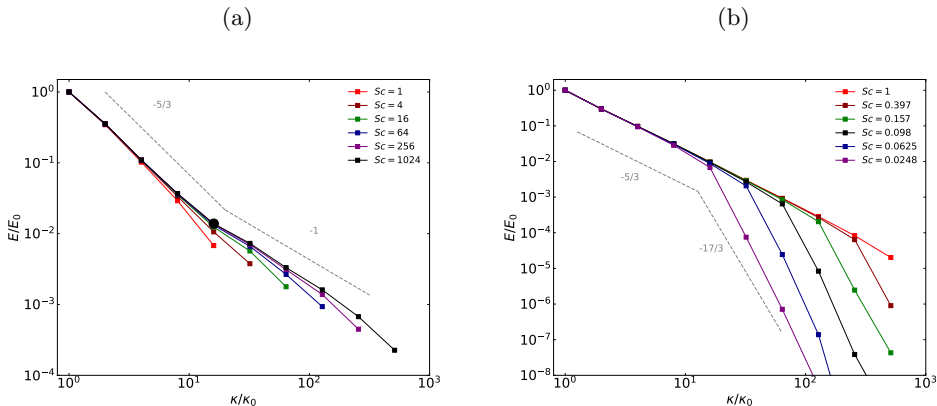


Figure 8: Scalar variance spectra for (a) $Sc \geq 1$, and (b) $Sc \leq 1$.

scale-length scale relationship is imposed, but as Kerstein (2013) notes “scalar cascading in HiPS is an outcome rather than a prescribed behavior, so the nature of that cascading in HiPS must be ascertained.”

It is seen that HiPS does in fact exhibit the $-5/3$ wavenumber power-law of the scalar spectrum. While HiPS does not prescribe the cascading behavior, its formulation is consistent with it, as HiPS subsumes the key phenomenology that governs it. This is evident as HiPS eddies result in local scale reduction, the eddy rate increases with decreasing level length giving quasi-stationary behavior, and the HiPS eddies are non-dissipative at all scales greater than l^* .

Figure 8a shows simulations for scalars with $Sc \geq 1$. Six Sc values are included. These have $Sc = 1, 4, 16, 64, 256, 1024$, corresponding to integer values of $\Delta i = i_s^* - i^*$ from 0 to 5, see (2.19). The simulation has a total of 12 levels and $i^* = 4$. This accommodates both a significant wavenumber range of the inertial-advective regime and extension to smaller scales ($i > i^*$) for $Sc > 1$. The simulations were run for $t = 1000\tau_0$, and flow states spaced by time intervals τ_0 were processed beginning with $50\tau_0$.

All spectra show a clear transition between the inertial-advective regime and the viscous-advective regime and they all obey the $-5/3$ scaling at low wavenumbers. In the viscous-advective regime $i > i^*$, the spectra show the expected κ^{-1} scaling. This is most obvious for the scalars with the highest Sc .

In the simple micromixing model used in this study, immediately after a swap occurs at level i_s^* , all parcels in the left subtree of the node at the given eddy level are mixed to their mean value in that subtree; all parcels in the right subtree are similarly mixed. This results in no scalar variance among parcels at levels greater than i_s^* , so the scalar variance spectrum is effectively chopped at length scales below l^* , corresponding to levels $i > i_s^*$. As formulated, this eliminates the need to implement any eddy events at levels $i > i_s^*$ because they would have no effect.

This, however, provides an inadequate representation of the inertial-diffusive scaling range, for which Batchelor (1959) predicted a $-17/3$ spectral scaling. This scaling was demonstrated by Chasnov & Rogallo (1988) and Chasnov (1991) using simulations of scalar transport in a frozen, Gaussian, isotropic velocity field, and in LES of decaying and forced turbulence. More recently, DNS by Yeung & Sreenivasan (2013, 2014) found the $-17/3$ spectral scaling in forced homogeneous isotropic turbulence with an imposed mean scalar gradient.

Accordingly, the $Sc < 1$ eddy event, which performs the described mixing if the event level is i_s^* , is modified in order to approximate the theoretical spectral scaling in lieu of the sharp cutoff at level i_s^* . Instead of assuredly mixing the respective two subtrees of the level- i_s^* event apex, for any eddy event at level $i \geq i_s^*$, both the left and right subtrees of the event apex are individually mixed with probability p based on a Bernoulli trial. This allows scalar fluctuations to persist below the Obukhov-Corrsin scale. At level $j > i_s^*$, we then have an inhomogeneous scalar fraction q^j where $q = 1 - p$. The scalar variance then would be q^j times what it would be in a $-5/3$ spectrum. Here it is assumed that the inertial-advective cascade proceeds as usual in the successive generations of unmixed subtrees, which requires the re-introduction of eddy events at levels $j > i_s^*$ where such events can change the system state (versus the absence of such events for $q = 0$). Recalling that spectral amplitude scales in proportion to the scalar variance, the $-17/3$ power-law spectrum scaling is obtained by imposing the requirement

$$\frac{E_j}{E_{i_s^*}} = \frac{\text{var}_j \phi}{\text{var}_{i_s^*} \phi} = q^j \left(\frac{\kappa_j}{\kappa_{i_s^*}} \right)^{-5/3} = \left(\frac{\kappa_j}{\kappa_{i_s^*}} \right)^{-17/3}. \quad (3.18)$$

Now, $l_s^*/l_j = 2^j$, so $\kappa_j/\kappa_{i_s^*} = 2^j$, and $j = \log_2(\kappa_j/\kappa_{i_s^*})$. Using this and solving the above equation for q gives $q = 2^{5/3-17/3} = 0.0625$ and $p = 1 - q = 0.9375$. This result is approximate because it is based on strict mean-field Kolmogorov phenomenology, omitting fluctuation effects such as backscatter (discussed with reference to the viscous-advective regime) that are inherent to HiPS.

On this basis, figure 8b shows simulation results for $Sc < 1$ in the inertial-diffusive regime. Each case again includes 12 tree levels and was run for the same time with the same number of flow states processed as the cases shown in figure 8a. That figure had $i^* = 4$ for $Sc = 1$, with higher levels accommodating larger Sc . For $Sc < 1$ in figure 8b, $i^* = 9$ for $Sc = 1$ (with levels starting at 0), and $Sc = 1, 0.397, 0.157, 0.0625, 0.0248$, and 0.098 (rounded), corresponding to $\Delta i = i_s^* - i^*$ from 0 to -5, respectively. The slopes in the inertial-diffusive regime are slightly steeper than $-17/3$, but they can be brought into agreement with this exponent by using a slightly lower value of p (around 0.9).

$p < 1$ allows gradual imposition of homogeneity to compete with swap-induced introduction of inhomogeneity such that the balance can be tuned to reproduce $-17/3$ scaling. This compensates for the underlying instantaneous nature of state changes in the model, a model artifact that introduces a splitting error. LEM is subject to a comparable artifact, producing an exponent error that has been explained quantitatively (Kerstein 1991b), but the LEM formulation does not accommodate a convenient correction.

The scalar spectra discussed above and plotted in figure 8 are discrete. As an alternative formulation, we can evaluate continuous spectra in the inertial-advective regime, which is convenient for analysis. This is done using a power-law with an exponent of $-5/3$, consistent with the presented spectra. The power-law amplitude is set so that the integral of the continuous spectra, extending to level 1 corresponding to L_I , recovers the total variance. Using such continuous spectra, we denote the compensated spectrum $E\kappa^{5/3}$ as $E_{\kappa 53}$; its nondimensional value is

$$\frac{E_{\kappa 53}}{\Delta\phi_0^2/L_0^{2/3}} = 4.3. \quad (3.19)$$

This is based on a simulation with $N_t = 12$ levels and $Sc = 1$, but applies generally given the collapse of the scalar spectra in the inertial-advective range, evident in figure 8.

4. Empirical correspondence

Equation (3.16) expresses the physical parameter Re_λ in terms of the model parameters Re and Sc . In conjunction with the equivalence of model and physical Sc values (see Appendix B), this enables quantitatively consistent comparison to DNS, as in Figure 7a.

Beyond this, it is of interest to quantify the relationships between model and physical values of various flow properties. Given reference scales L_0 , τ_0 , and $\Delta\phi_0$, a HiPS simulation is defined in terms of Re , Sc , and the dimensionless scalar gradient G . All other dimensionless quantities will be functions of these.

In previous sections, we evaluated the mean scalar dissipation rate, turbulent diffusivity, and amplitude of the compensated inertial-range spectrum. They are reproduced here for convenience and denoted C_χ and C_D , and C_E , respectively:

$$\frac{\langle\chi\rangle}{\Delta\phi_0^2/\tau_0} = C_\chi = \frac{1}{2}, \quad \frac{D_T}{L_0^2/\tau_0} = C_D = \frac{1}{16}, \quad \frac{E_{\kappa 53}}{\Delta\phi_0^2/L_0^{2/3}} = C_E = 4.3. \quad (4.1)$$

The scalar spectrum has the model form $E(\kappa) = \beta\langle\chi\rangle\epsilon^{-1/3}\kappa^{-5/3}$. Solving this for the kinetic energy dissipation rate ϵ and using $\beta = 0.7$ as the Obukhov-Corrsin constant (Donzis *et al.* 2010) gives

$$\frac{\epsilon}{L_0^2/\tau_0^3} = \left(\frac{\beta\langle\chi\rangle}{E_{\kappa 53}}\right)^3 / \frac{L_0^2}{\tau_0^3} \equiv C_\epsilon = 0.00054. \quad (4.2)$$

Donzis *et al.* (2010) performed DNS of passive scalar mixing in homogeneous turbulence with a mean scalar gradient, corresponding to the HiPS simulations considered here. They report a sharp transition from inertial-advective to viscous-advective spectrum scaling at $\kappa^*\eta \approx 0.05$. Using $\kappa^* = 2\pi/l^*$ gives

$$\frac{l^*}{\eta} = C_\eta = 126. \quad (4.3)$$

We adopt this value for calibration, noting however that measurements not precisely equivalent to the DNS setup yield $C_\eta \approx 20$ (Hill 1978).

Appendix B gives the HiPS viscosity as $\nu/(L_0^2/\tau_0) = A^{4N^*/3}/(2(2 - A^2))$. This can be compared to a physical viscosity $\hat{\nu}$ using the definition of η as $\eta = (\hat{\nu}^3/\epsilon)^{1/4}$. Then (4.2), (4.3), and $l^* = L_0A^{i^*} = L_0A^{N^*-3}$ give $\hat{\nu}/(L_0^2/\tau_0) = (C_\epsilon/C_\eta^4)^{1/3}A^{4N^*/3}/A^4$. The ratio $\nu/\hat{\nu}$ is then

$$\frac{\nu}{\hat{\nu}} = \frac{A^4}{2(2 - A^2)} \left(\frac{C_\eta^4}{C_\epsilon}\right)^{1/3} = C_\nu = 139 \quad (4.4)$$

for $A = 0.5$. It was noted that the physical Sc must equal the HiPS Sc for consistent representation of the scalar transport regimes. Hence, $D/\hat{D} = \nu/\hat{\nu}$.

As explained in Appendix B, individual HiPS transport coefficients scale with the frequency of mixing events. Their adjustability thus reflects the freedom in HiPS to rescale time without affecting single-time ensemble statistics (assuming

statistical stationarity), as implied by a related discussion in § 2.3.1. For the time-developing process examined in § 3.2, a completely different calibration approach is adopted in which time-rescaling freedom allows model time to be calibrated relative to physical time.

5. Discussion and conclusions

5.1. Model extensions

Hierarchical parcel swapping (HiPS) was originally introduced as a formulation designed to time advance unity- Sc diffusive scalar fields advected by parametrically specified inertial-range turbulence (Kerstein 2013), extensible to turbulent flow simulation by introducing a vector velocity field (Kerstein 2013, 2014). Here, extension to nonunity Sc has been achieved by means of two model extensions.

For $Sc > 1$, the viscous regime has been incorporated by adopting the time scale of the smallest turbulent eddies as the advective time scale governing swap occurrences at all length scales below the inertial range, where such swaps idealize the viscous-range effects of the smallest inertial-range eddies rather than (nonexistent) smaller-scale eddies. On this basis, the HiPS tree has been extended to the Sc -dependent Batchelor scale η_b , at which each pair of adjacent parcels is mixed as needed to maintain compositional equivalence.

For $Sc < 1$, the Obukhov-Corrsin scale exceeds the transition scale l^* from inertial to viscous scaling so mixing is introduced within the subrange $[\eta_{oc}, l^*]$ of the inertial range. This generalizes the enforcement of the compositional uniformity of parcel pairs to imposition of this requirement on larger subtrees with the caveat that this nonlocal form of mixing is applied with probability less than unity when a de-homogenizing change occurs, where this *ad hoc* procedure serves to enforce $-17/3$ spectral scaling in the inertial-diffusive scale range.

For any Sc , the HiPS tree can be extended as far down in scale as desired provided that the appropriate degree of compositional uniformity is enforced below scale l_b . In principle, the ideal tree structure can accommodate any number of scalars with no bounds on the associated Sc values.

These model extensions serve two purposes. First, they are the basis for study of flow and mixing physics that are captured by the model. Second, they broaden the scope of scientific and practical applications of the model. Present contributions that fall within the respective categories are summarized.

5.2. Physics investigations and results

The practical step of extending HiPS into the viscous range in order to accommodate high- Sc scalar fields extended the HiPS representation of turbulence phenomenology in several ways. First, the analytical tractability of HiPS viscous-range parcel-pair dispersion led to a closed-form solution for pair-separation PDF evolution in conformance with theory (Lundgren 1981), establishing the quantitative accuracy of the balance of drift and diffusion mechanisms governing dispersion. Second, by introducing viscous-range swaps that represent the effects of physical eddies on smaller-scale scalar structures that are not subject to comparably small eddies, distant interactions were introduced that capture a subtle large-deviation property of scalar dissipation.

The swaps alone, which are simply displacements of subtrees within the HiPS tree structure, have been shown to capture much of the phenomenology of parcel-

pair dispersion within and across the viscous and inertial ranges. A notable distinction between the HiPS treatments of dispersion and scalar mixing is that Lagrangian dispersion requires a spherically symmetric treatment in HiPS while the mean scalar gradient is imposed using a boundary condition that requires the physical interpretation of this HiPS setup as a line of sight aligned with the gradient. The distinct treatments of these two applications are discussed in Appendix A.

For the viscous regime of pair dispersion, the model similarity solution has been shown analytically to match the theoretical result of Lundgren (1981) with near-exact precision. The model similarity solution for the inertial regime exhibits minor deviations from Lundgren’s semi-empirical formula. The model solution for pair-dispersion PDF evolution initialized as in the DNS of Scatamacchia *et al.* (2012) is in reasonable quantitative agreement with the evolution produced by the DNS, notably including the cross-coupling of viscous-range and inertial-range phenomenology. This indicates that no bespoke transitional treatment is required in order to capture the cross-coupling. The quantitative comparison relies on parameter calibration using Lundgren’s formula, the empirical Richardson constant, and an empirical Reynolds number relating transport by the smallest turbulent eddies to the nominal dimensionally prescribed value.

Notably, the tail behavior of the PDF of scalar-variance dissipation is found to be in conformity with a high- Sc theoretical prediction of a stretched-exponential shape based on analysis of scalar intermittency induced by non-intermittent narrowband stochastic advection (Chertkov *et al.* 1998). The analysis is based on the scalar transport equation subject to stochastic forcing of scalar fluctuations and a stochastic solenoidal velocity field. The present results indicate that the theoretically predicted intermittency scaling might not be uniquely contingent on the standard continuum form of scalar transport, but instead could have a deeper origin that is captured by a minimal mathematical abstraction of advection-diffusion phenomenology.

In this context, it is instructive to revisit the HiPS representation of viscous-range distant-interaction effects. A small viscous-range scalar structure is subject to order-unity scale reduction under the influence of a Kolmogorov-scale eddy. In HiPS, this is emulated by implementing a swap at the scale of the structure. A sequence of such swaps lacks the coherence resulting from the simultaneous action of the eddy on structures at all scales below the eddy size. The HiPS results suggest that this coherence is not a leading-order influence on the functional form of the tail of the dissipation PDF, raising the question of whether this inference can be directly confirmed by some form of analysis.

The viscous-range swaps that represent distant interactions in HiPS are formally equivalent to the inertial-range swaps that represent individual turbulent eddies, the only difference being the level dependence of swap rates in the inertial range in contrast to the lack of such dependence in the viscous range. Therefore, it is reasonable to expect some degree of qualitative consistency of the HiPS viscous-range and inertial-range ($Sc = 1$) PDF shapes. The most remarkable but as yet unexplained outcome is that HiPS yields the same exponent value $1/3$ for both regimes. Given that the exponent value has empirical support for both regimes as well as theoretical support for the viscous regime, it is of particular importance to seek an explanation of these observations that improves on previous speculative proposals (Chertkov *et al.* 1998). Finally, an abstraction of HiPS phenomenology

that transparently demonstrates the origin of the HiPS stretched-exponential tail has been presented in Appendix E.

This raises the broader question of the HiPS representation of inertial-range scalar intermittency. A suggestive indication is that LEM has been shown to reproduce scalar structure-function exponents with reasonable quantitative accuracy over a significant range of structure-function orders (Kerstein 1991b). This has been explained by an analysis (Kalda & Morozenko 2008) that suggests some commonality with the HiPS representation of inertial-range phenomenology. The implications of these observations will be addressed elsewhere.

5.3. *Capability development for applications*

DNS data has been used to calibrate coefficients that relate model scalar power-spectrum amplitudes and transition wavenumbers to their physical counterparts. This will enable future quantitative application of the model to flow configurations of interest.

The extension to nonunity Sc enables model application to heat transfer with nonunity Pr and further model extension to reacting flows subject to the effects of multi-stream mixing and differential diffusion. For these applications, it remains to be determined whether HiPS will have overall cost/performance advantages relative to the triplet-map-based methods LEM and ODT, whose resolution of scalar diffusion in 1D physical space is costly but provides high fidelity for combustion and related applications (Kerstein 2022).

One pertinent consideration is that, as in HiPS, the triplet map imposes order-one multiplicative scale reduction, but unlike a HiPS swap, one triplet map can unphysically increase pair separation by an arbitrarily large multiplicative factor. Consequently, LEM and ODT cannot match the high-fidelity HiPS dispersion phenomenology that is demonstrated in § 3.2.

The most important future extension of HiPS is incorporation of the newly introduced features into flow HiPS (Kerstein 2014, 2021). This can broaden the range of flow phenomena that can be amalgamated into a unitary modeling framework. Suitability for this future work was a consideration in the formulation of the present version of the model, as explained in Appendix A.

In contrast to present and future model extensions, a minimal configuration is used to highlight the simplicity of HiPS advancement in Appendix D. After an initial transient, the system toggles between two states. This enables the use of enumeration of cases to evaluate turbulent flux, production, and scalar dissipation subject to a mean gradient imposed by a boundary condition that enforces statistical stationarity. This demonstrates the irreducible simplicity of the HiPS advection and mixing treatments. In this sense, the highest degree of abstraction that can usefully represent a variety of turbulent mixing processes within an unsteady, spatially localized framework has been established.

A feature that will facilitate the use of HiPS for applied studies is its formal resemblance to existing mixing models. In particular, subgrid-scale mixing closures of conventional under-resolved three-dimensional flow computations typically involve a collection of parcels that are mixed either pairwise or with the notional mean parcel composition (Fox 2003). Pairwise mixing can be based on random parcel pairings (Curl 1963) or pairing weighted by the similarity of parcel compositions (Subramaniam & Pope 1998). To the extent that time advancement of the PDF of parcel compositions is sufficient to close the flow computation, the role of HiPS would be to introduce turbulence phenomenology into the selection of parcel

pairs to be mixed. Thus, the time-advancement operations need no modifications other than a different source of the inputs that specify which parcels should be selected to be mixed. The previously documented computational efficiency of HiPS numerical implementation (Kerstein 2014) indicates its practicality as a subgrid closure. This offers the prospect of a straightforward remedy for longstanding deficiencies of existing mixing closures (Fox 2003).

Acknowledgment. The authors thank P. K. Yeung and D. Dotson for helpful guidance.

Funding. H.S. acknowledges support by the German Federal Government, the Federal Ministry of Research, Technology and Space, and the State of Brandenburg within the framework of the joint project EIZ: Energy Innovation Center (project numbers 85056897 and 03SF0693A) with funds from the Structural Development Act (Strukturstärkungsgesetz) for coal-mining regions.

Declaration of Interests. The authors report no conflict of interest.

Appendix A. Symmetry, dimensionality, and scale discretization

The scale-reduction parameter A and its association with the effective physical-space dimensionality d of the HiPS tree are discussed in § 2.2. The reasoning is based on the multiplicative increase of the number of parcels as levels are added to a HiPS tree for a given A value. This does not directly imply that the choice of A is consequential for a given model instantiation, other than that A controls the number of levels needed to span a particular scale range such as $[l^*, L_0]$. In this context the choice of A is ostensibly of minor importance, serving for instance to control the number of data points appearing in the spectra curves plotted in figure 8. However, it is more broadly consequential, as discussed below (3.4).

To clarify the influence of the choice of A , a notional swap-based formulation of pair dispersion in 3D physical space is outlined. Suppose that the flow domain in 3D continuum space is discretized into equal-volume spherical shells concentric with one of the two advected particles. Then a swap of any two sets of shells requires the shell thickness as well as the inner radius of each shell to change in order to preserve volumes. Our sole concern is the time history of the distance r of the second particle from the first particle at the origin. Owing to the equi-volume partition of the flow domain, r is uniquely determined by, albeit not proportional to, the number of shells between the second particle and the origin.

The HiPS version of this formulation is analogous, except that the set of possible values of r is finite based on the HiPS topological definition of pair separation. Multiple shells have the same r value, but given an initial condition of equi-volume parcels that sum within each subtree associated with given r to the appropriate subtree volume, the volume-preserving shell displacements satisfy conservation of pair-separation probability. This assures that the steady-state condition of spatially uniform probability density of the second-particle location expressed in terms of r is satisfied.

This geometrical picture corresponds to a specialization of the ‘reduced’ HiPS formulation shown in figure 1 of Kerstein (2021). The location of the second particle is referenced to the location of the first particle, which is therefore held fixed at the location of the leftmost parcel to avoid repeated coordinate transformations. This prohibits swaps containing the first particle. The number of parcels in each successive subtree corresponding to the next larger r value is double the preceding number, so the associated subtree volumes likewise double. The ratio of the r value of one such subtree to the next defines the level length-

scale stride A . Thus, A is the ratio of radii associated with two successive subtree volumes. Those volumes scale as $(Ar)^3 - (A^2r)^3$ and $r^3 - (Ar)^3$, respectively, where, for convenience, the innermost radius is designated as A^2r . As noted, the latter subtree volume is twice the former, yielding $A = 2^{-1/3}$. This reasoning geometrically instantiates the explanation in § 2.2.

Importantly, the present application to pair dispersion does not involve Monte Carlo implementation of HiPS *per se*, but rather, evolution equations governing the pair-separation PDF parameterized by the level index k supplemented by a geometrically based transformation to the r coordinate that identifies the required A value. The reduced HiPS formulation does not capture the full HiPS phenomenology (Kerstein 2021) but for pair dispersion a fully equivalent reduced version can be formulated, thereby reducing the number of required parcels to the number of tree levels. As will be reported elsewhere, this will enable low-cost Monte Carlo pair-dispersion simulations. This is useful because outputs of interest that are accessible only by means of Monte Carlo simulations, such as first-passage times and level-crossing statistics, can then be obtained.

To adapt this reasoning for application to advected scalar fields, the cylindrical temporally developing (meaning statistically homogeneous in the axial direction) jet is considered. The leftmost parcel pair represents the initial jet flow with the first parcel interpreted as an axially aligned circular cylinder while successive parcels represent cylindrical shells. The cylinder and successive shells all have the same cross-sectional area such that for a given fixed cylinder height z (which in DNS would be the axial domain length, with periodic boundary conditions applied axially) they are all equi-volume and therefore suitable for conservative swapping. As in the case of spherical symmetry, the proximity criterion aggregates parcels into equal- r groups such that the number of parcels per group doubles for each factor of $1/A$ increase of r . Applying the same analysis as for the spherical case but with the $zr dr$ volume-element scaling rather than the spherical $r^2 dr$ scaling, the result $A = 2^{-1/2}$ is obtained.

This cylindrical formulation enables time advancement of the radial distribution of a scalar field initially confined to a radial interval representing the jet nozzle outflow. Analogous considerations apply to the planar jet issuing from a notionally unbounded rectangular slot, yielding $A = 1/2$.

Different considerations apply to the present HiPS application involving a jump-periodic scalar boundary condition. The scalar-field deviation from the mean is axially homogeneous and homogeneous in planes normal to the imposed axial mean scalar gradient, but unlike the flow field it is anisotropic.

Unlike the jet examples that evolve the scalar field in a coordinate normal to the axis, HiPS evolves the scalar field along a representative axial line of sight. For this setup, the parcels in each of the HiPS half-trees are nominally at the same axial location so the only identified axial separation is between parcels that are in different half-trees, corresponding to separation $L_0/2$. Thus, only the largest possible swap size can induce nonzero axial displacements. Smaller-scale swaps nominally involve axially collocated parcels, so the tree structure at smaller scales serves only to identify parcel pairs or groups that are subject to mixing. In this context, A is relevant only for discretizing scales from a wavenumber viewpoint and its value serves mainly to control the wavenumber stride of discrete spectra such as those shown in figure 8.

However, A is relevant for the largest swap involving axial displacements $\pm L_0/2$ of size- $L_0/4$ quarter-trees. Because the swaps are conservative, the absence of

parcel-width adjustment upon axial physical-space displacement implies that parcel volumes scale linearly with parcel size. In effect, swaps of quarter-trees are treated as though they were axial displacements of unbounded planar slabs of width $L_0/4$. The equivalence of this formulation to the planar-jet case indicates that $A = 1/2$ holds for the former as well as the latter.

An A value corresponding to non-Cartesian symmetry would imply a specified coordinate origin, but if it were chosen to be at the center of the HiPS domain then all parcels would be at the same absolute distance from that origin, so when a parcel is displaced from one half-tree to the other, no change in parcel width is implied. Although any A value would thus be operationally valid, the stride $A = 1/2$ was applied in this study, yielding an economical, conceptually transparent formulation. This choice was additionally motivated by anticipation of the future incorporation of the current mixing-HiPS formulation into flow HiPS as previously (Kerstein 2014) implemented, for which flow inhomogeneity along the HiPS line of sight imposes the choice $A = 1/2$. That model formulation indicated some performance degradation when using other A values. Experience with subgrid-scale closures involving map-based advection (Kerstein 2022) likewise supports the preference for a planar-symmetric formulation.

Appendix B. Evaluation of HiPS molecular-transport coefficients

In HiPS, Sc is a parameter that is used to specify ratios of length scales that demarcate regime transitions. It has been noted that consistency with the scaling laws governing transitions between scalar-transport regimes requires Sc in HiPS to be the same as the physical Sc value. For present model applications, this avoids the need to specify the values of the individual molecular-transport coefficients in the physical definition $Sc = \nu/D$. However, future model applications will require these values and they are of present relevance to the evaluation of the relationship between their model values and respective physical values in § 4. Therefore, a derivation of their values is presented.

Although viscosity has no direct role in the current model formulation, evaluation of the HiPS value of D for given Sc yields the implied viscosity value $\nu = ScD$. We denote the value of D for $Sc = 1$ as D_1 , with $\nu = D_1$.

The present HiPS formulation can accommodate multiple scalars encompassing an arbitrary range of Sc values. This general setting is adopted so that the analysis that follows is as widely applicable as possible. In this context, termination of the HiPS tree at any finite number N_t of levels cannot accommodate all cases of possible interest. Therefore a notional infinite-depth tree is assumed.

In HiPS, $Sc < 1$ is implemented by introducing homogenization of subtrees emanating from tree level i_s^* , corresponding to length scale l_s^* . On an infinite-depth tree, subtree homogenization is required for all scalars. Indeed, even on a finite-depth tree with multiple scalars that have unequal diffusivities, including at least one high- Sc scalar, all other scalars except possibly the highest- Sc scalar must be subject to subtree homogenization. Therefore this modification of the model has practical as well as conceptual relevance.

$Sc < 1$ scalars deviate from this formulation in that homogenization is implemented with probability $p < 1$. The analysis that follows can be extended to accommodate this but then it is not fully consistent with $Sc = D_1/D$. Since p is close to unity, the inconsistency is quantitatively small, but practical applications might not be sensitive to the difference between the $-17/3$ inertial-diffusive

spectral scaling and a sharp cutoff at length scale l_s^* , so p can be set to unity to avoid the discrepancy. This will be handled on a case-specific basis in future model applications.

A related detail is that l_s^* will not generally correspond to a level length scale l_i . The analysis below can be extended to accommodate this using the approach in § 2.5.3, but since the relevant points are captured by assuming exact correspondence, this extension is not presented here.

On this basis, the HiPS analog of the molecular diffusivity of a $Sc = 1$ (hence $l_s^* = l^*$ and $i_s^* = i^*$) scalar, D_1 , is evaluated. Namely, random-walk theory is applied to the displacements of a notional molecule of the scalar species that are implied by the sequence of homogenization instances during HiPS advancement. As explained in Appendix A, we adopt a line-of-sight interpretation of the HiPS domain, so the diffusivity is based on 1D random-walk theory. (In § 3.4 the turbulent diffusivity is similarly evaluated, albeit on the basis of swap-induced parcel displacements rather than mixing-induced molecule displacements.)

Accordingly, the diffusivity is evaluated as $D_1 = \overline{R^2}/2\tau$, where $\overline{R^2}$ is the mean square displacement of fluid undergoing mixing, and $\tau = \tau^*$ is the mean time between displacements. A notional molecule in a parcel within a subtree undergoing homogenization is deemed equally likely to reside in any of the subtree parcels after homogenization, therefore, the number of possible displacements equals the number of parcels in the subtree (including a zero-distance displacement for molecules remaining in their original position).

In figure 1, consider homogenization over the eight parcels in the left half-tree with $i_s^* = 0$. The scalar in parcel a , for instance, would be spread across all eight parcels with displacement magnitudes of 0 (no motion to parcel a), $l_s^* A^4$ (parcel b), $l_s^* A^3$ (parcels c and d), and $l_s^* A^2$ (parcels e - h). Note the degeneracy of displacement due to the definition of parcel proximity. In general, the mean square displacement is given by $\overline{R^2} = \frac{l_s^{*2} A^4}{2^{J+1}} \sum_{j=0}^J 2^j (A^2)^{J-j}$, where the sum ranges over nonzero displacement magnitudes, from $j = 0$, corresponding to the nearest-neighbor separation, to the largest displacement $J \equiv N_t - 3 - i_s^*$, which is equal to the number of levels between i_s^* and the parcel grandparent level. (The normalization preceding the sum includes the zero-displacement case.) In the above example referencing figure 1 with $i_s^* = 0$, we have $N_t = 5$ and $J = 2$. Using the sum of a geometric series, the above equation simplifies to $\overline{R^2} = \frac{1}{2} l_s^{*2} A^4 \left(\frac{2}{A^2} - \left(\frac{2}{A^2} \right)^{-J} \right) / \left(\frac{2}{A^2} - 1 \right)$.

As noted, the unique universally applicable case is $N_t = \infty$, and the finite depth used in numerical applications introduces spatial-discretization error. Specializing $\overline{R^2}$ to the limit of infinite J gives $\overline{R^2} = l_s^{*2} A^4 / (2 - A^2)$. Combining results, and using $D = D_1 / Sc$ gives

$$\frac{D}{l_s^{*2} / \tau^*} = \frac{A^4}{2(2 - A^2) Sc}, \quad (\text{B1})$$

corresponding to

$$\frac{D}{L_0^2 / \tau_0} = \frac{A^{\frac{4N^*}{3}}}{2(2 - A^2) Sc}. \quad (\text{B2})$$

Although these results systematically quantify the molecular transport associated with HiPS mixing, this does not guarantee the physical fidelity of the inferred results. The conditioning of the occurrence of molecular transport on advection

events in HiPS is not causally correct. Nevertheless, the overall behavior is phenomenologically self-consistent, as indicated by the reported results. Viscosity was similarly inferred with reasonable accuracy from HiPS mixing in Kerstein (2014), albeit computationally rather than analytically.

Appendix C. Analysis of the time advancement of the PDF of parcel-pair separation

To compare (3.2) to conventional representations of pair-dispersion statistics, that equation is approximated by treating k as continuous and Taylor expanding the right-hand side. First, (3.2) is multiplied by $2B^{1-k}$, giving

$$2B^{1-k} \frac{dP_k}{dT} = 2BP_{k-1} - (2+B)P_k + P_{k+1}. \quad (\text{C1})$$

Substitution of the Taylor expansion $P_{k\pm 1} = P_k \pm \frac{dP_k}{dk} \Big|_k + \frac{1}{2} \frac{d^2P_k}{dk^2} \Big|_k$ into (C1) gives

$$2B^{1-k} \frac{\partial P_k}{\partial T} = (B-1)P_k - (2B-1) \frac{\partial P_k}{\partial k} + \left(B + \frac{1}{2}\right) \frac{\partial^2 P_k}{\partial k^2}. \quad (\text{C2})$$

(Note that in the Taylor expansion, the k -space interval $\Delta k = (k+1) - k = 1$ is used.) At this point the truncation of the expansion at second order is arbitrary but its validity is addressed in what follows.

Equation (C1) is specialized for application to the viscous range by setting B equal to unity, which has the same effect in (C2) as setting $\tau_k = \tau^*$ for all k . Importantly, this decouples B from its definition in terms of A . The underlying model still depends on $A < 1$ through the A dependence of the eventual conversion from k to r . On this basis, (C2) reduces to

$$\frac{\partial P_k}{\partial T} = -V_d \frac{\partial P_k}{\partial k} + D_d \frac{\partial^2 P_k}{\partial k^2}, \quad (\text{C3})$$

where $V_d = 1/2$ and $D_d = 3/4$. The solution for $P_k(T=0) = \delta(k-1)$ is

$$P_k = \frac{1}{(4\pi D_d T)^{1/2}} \exp[(k-1 - V_d T)^2 / (4D_d T)]. \quad (\text{C4})$$

Next, P_k is converted to $P(r)$ where r is the physical-space parcel separation corresponding to level k . The probability in the k interval $\Delta k = 1$ is $P_k \Delta k = P_k$, which must equal the same probability expressed as $P(r) \Delta r$, where $\Delta r = r - Ar$. Then $P(r) = P_k \Delta k / \Delta r$. The parcel-pair separation is $r = L_0 A^{N_t - k}$, or $r = r_1 A^{1-k}$, where $r_1 = r(k=1)$. Again treating k as continuous, $\Delta k / \Delta r$ is evaluated as $dk/dr = [r \ln(1/A)]^{-1}$, and $P(r)$ is lognormally distributed:

$$P(r) = \frac{1}{r(4\pi \hat{D}_d T)^{1/2}} \exp\left(\frac{[\ln(r/r_1) - \hat{V}_d T]^2}{4\hat{D}_d T}\right). \quad (\text{C5})$$

Here, $\hat{V}_d = V_d \ln(1/A)$, and $\hat{D}_d = D_d [\ln(1/A)]^2$, retaining dependence on A .

For bounded r , as in any computation, the tails of the PDF are truncated and the solution between the bounds deviates from lognormal form. For these reasons, computed PDFs $P(r)$ must be scaled by a time-dependent normalization factor.

Lundgren (1981) likewise obtains lognormally distributed $P(r)$ for the viscous

range, but his theory yields a different differential equation whose solution gives the result $\hat{V}_d/\hat{D}_d = 3$, while the HiPS value is $2/[3 \ln(1/A)]$. The Lundgren value is matched for $A = \exp(-2/9) = 0.8$. Dimensional considerations discussed in § 3.2.2 yield the requirement that $A = 2^{-1/3}$, which is fortuitously within 1% of 0.8.

Thus, HiPS yields a unique prediction of viscous-range self-similar pair-separation PDF evolution in three dimensions that is in near-exact agreement with Lundgren’s result. However, Lundgren (1981) obtains the same viscous-range result for two as for three dimensions, while for $d = 2$ HiPS requires $A = 2^{-1/2} = 0.71$, which confirms that the exactitude of the agreement with Lundgren (1981) for $d = 3$ is fortuitous. In this regard, the lack of A dependence of P_k when (C1) is specialized to the viscous range highlights the distinction between the internal consistency of HiPS and the issues that arise when transforming to physical space.

Regarding the accuracy of the Taylor-series truncation in (C2), the discussion of figure 4a highlights the close agreement between the analytically derived PDF for the viscous range and the exact numerical result. A more definitive test is comparison of the equilibrium PDF shape obtained from the specialization of (C2) to stationarity and the exact equilibrium result, (3.3). (To verify that stationarity corresponds to equilibrium, note that the exact equilibrium result satisfies (C1) with the left-hand side set equal to zero.) For the viscous range, substitution of $B = 1$ and the *ansatz* $P_k \propto q^k$ into (C2) yields the stationary solution $q = \exp(2/3) = 1.95$. Comparison to the exact equilibrium result $P_k \propto 2^k$ indicates that, at least for this regime, the Taylor-series truncation is fairly accurate albeit inexact.

Relaxing the $B = 1$ restriction yields a B -dependent stationary solution of (C2), with $q = 2$ only for A close to 0.6. For the A values of interest, the deviations from the exact stationary solution are not large, but this is immaterial. The only tangible present benefit of (C2) is that its specialization to (C5) transparently exhibits the dispersion phenomenology in a manner that led to the parameter assignment $A = 0.8$ and thus to predictive capability across scaling regimes.

The inertial-range dependence of level time scales on level length scales is introduced into (C2) by substituting $B = A^{2/3}$. In this case, that equation has no closed-form solution. As in § 3.2.3, the approximation inherent in the derivation of C2 is avoided by solving (3.2) for P_k using the same initial and boundary conditions as for the viscous-range solution.

The basis of Richardson scaling of HiPS dispersion is indicated by rewriting $B^k dT$ in (C1) as dS , where $S = B^k T$ is a similarity variable that subsumes the dependence of the time advancement on both T and k . The separation distance corresponding to separation index k is $L_0 A^{N_t - k}$ so the inertial-range *ansatz* $B = A^{2/3}$ that introduces the length-scale dependence of the eddy rate into (C1) imposes Richardson similarity by construction.

Appendix D. Analysis of mixing in a three-level tree

The HiPS flux, production, and dissipation are evaluated directly for a three-level tree. Refer to table D1.

Let the four parcels have initial values $(0, 0)$, $(1, 1)$, where parentheses indicate half-trees, giving $\Delta\phi_0 = 1$. Only level-0 swaps are possible. With equal likelihood, a swap is either jump-periodic (JP), corresponding to flux between hypothetically

Table D1: HiPS state evolution for a three-level tree. Parentheses group parcel values in half-trees. EE refers to an eddy event involving a swap of type jump-periodic (JP) or internal (I) followed by mixing of parcel pairs. Subscripts on half-tree averages designate the different stages of evolution.

Initial state	(0,0), (1,1)							
$\langle\phi\rangle_0$			0		1			
$\langle\phi'^2\rangle_0$			0		0			
First EE: I or JP	I (applied to initial state)				JP (applied to initial state)			
After swap	(0, 1), (0, 1)				(-1, 0), (1, 2)			
After mixing	$(\frac{1}{2}, \frac{1}{2}), (\frac{1}{2}, \frac{1}{2})$				$(-\frac{1}{2}, -\frac{1}{2}), (\frac{3}{2}, \frac{3}{2})$			
$\langle\phi\rangle_1$	$\frac{1}{2}$		$\frac{1}{2}$		$-\frac{1}{2}$		$\frac{3}{2}$	
$\langle\phi'^2\rangle_1$	$\frac{1}{4}$		$\frac{1}{4}$		$\frac{1}{4}$		$\frac{1}{4}$	
Next EE: I or JP	JP		I		JP		I	
After swap	$(-\frac{3}{2}, \frac{1}{2}), (\frac{1}{2}, \frac{5}{2})$		$(\frac{1}{2}, \frac{1}{2}), (\frac{1}{2}, \frac{1}{2})$		$(-\frac{1}{2}, -\frac{1}{2}), (\frac{3}{2}, \frac{3}{2})$		$(-\frac{1}{2}, \frac{3}{2}), (-\frac{1}{2}, \frac{3}{2})$	
$\langle\phi\rangle_2$	$-\frac{1}{2}$		$\frac{3}{2}$		$\frac{1}{2}$		$\frac{1}{2}$	
$\langle\phi'^2\rangle_2$	$\frac{5}{4}$		$\frac{5}{4}$		$\frac{1}{4}$		$\frac{1}{4}$	
After mixing	$(-\frac{1}{2}, -\frac{1}{2}), (\frac{3}{2}, \frac{3}{2})$		$(\frac{1}{2}, \frac{1}{2}), (\frac{1}{2}, \frac{1}{2})$		$(-\frac{1}{2}, -\frac{1}{2}), (\frac{3}{2}, \frac{3}{2})$		$(\frac{1}{2}, \frac{1}{2}), (\frac{1}{2}, \frac{1}{2})$	
$\langle\phi\rangle_3$	$-\frac{1}{2}$		$\frac{3}{2}$		$\frac{1}{2}$		$\frac{1}{2}$	
$\langle\phi'^2\rangle_3$	$\frac{1}{4}$		$\frac{1}{4}$		$\frac{1}{4}$		$\frac{1}{4}$	
$\langle\phi\rangle_3 - \langle\phi\rangle_1$	-1	1	0	0	0	0	1	-1
$\langle\phi'^2\rangle_2 - \langle\phi'^2\rangle_1$	1	1	0	0	0	0	1	1
$\langle\phi'^2\rangle_3 - \langle\phi'^2\rangle_2$	-1	-1	0	0	0	0	-1	-1
Repeat, I or JP EE	...							

adjacent domain boundaries, or internal (I), corresponding to flux across the domain center. A JP swap adds ± 2 to the scalar value of each parcel deemed to exit and re-enter the domain, where the direction of displacement determines the sign of this adjustment. We can ignore permutations within a half-tree without loss of generality.

This three-level model implementation has distinctive features that do not apply to cases with four or more levels. Each eddy event produces one of two

distinct final system states: $(1/2, 1/2)$, $(1/2, 1/2)$, or $(-1/2, -1/2)$, $(3/2, 3/2)$, which are uniform and nonuniform, respectively. Starting from either of the two states, the system state is uniform after a type-I event and nonuniform after a type-JP event. The half-tree mean values $\langle\phi\rangle$, and variances $\langle\phi'^2\rangle$ after each of swap and mixing operations comprising the eddy event are shown in the table. $\langle\phi'^2\rangle$ is computed as the mean square difference between the parcel values in the half-tree and the imposed ensemble mean value (0 or 1) in the half-tree. An eddy event preceded by an eddy event of the same type produces no state change. In effect, the system evolves only when two events of different type occur in succession, so the evolution consists of switches from one state to the other.

Consider the flux through the domain center, arising from internal swaps. These result in $\langle\phi\rangle_3 - \langle\phi\rangle_1$ equal to 0 or -1 in the right half-tree, and 0 or 1 in the left half-tree. The average time between internal swaps is $2\tau_0$, so the average $d(\langle\phi\rangle_3 - \langle\phi\rangle_1)/dt$ in the right half-tree is $-1/(4\tau_0)$. Use of the reasoning in § 3.3 recovers the nondimensional flux of $-1/8$, equation 3.9.

The production \mathcal{P} is the average rate of change of variance due to swaps, which happen at mean rate $1/\tau_0$. This production is given by the mean (over the four columns of table D1) of $(\langle\phi'^2\rangle_2 - \langle\phi'^2\rangle_1)/\tau_0 = 1/(2\tau_0)$, which recovers the nondimensional production of $1/2$ that is shown in (3.13).

Similarly, $\langle\chi\rangle$ is the negative of the average rate of change of variance due to mixing occurrences, which happen at mean rate $1/\tau_0$. This dissipation is given by the mean (over the four columns of table D1) of $-(\langle\phi'^2\rangle_3 - \langle\phi'^2\rangle_2)/\tau_0 = 1/(2\tau_0)$, which recovers the nondimensional dissipation value $1/2$, equation 3.14.

Appendix E. Phenomenological basis of the dissipation PDF shape

A simple abstraction of HiPS advancement is formulated that crudely mimics HiPS phenomenology while providing analytical tractability. Note first that the type-JP swap (see Appendix D) preserves scalar deviation from the mean rather than the scalar value *per se*, analogous to the corresponding DNS boundary condition. For mathematical simplicity, periodicity is relaxed here and an individual Lagrangian parcel is deemed to perform a simple random walk with step size unity on a 1D domain while preserving the scalar value rather than the scalar deviation. This recasts the top-level JP swaps as purely advective displacements. With each step, the parcel scalar deviation Φ relative to an imposed mean scalar gradient of unity changes by ± 1 . After each step a mixing operation is performed with probability $1/2$ based on independent Bernoulli trials. If mixing is done, the parcel is mixed toward the local mean value by multiplying Φ by a fixed factor $h < 1$ that subsumes all HiPS mixing phenomenology in a simple parameterization. Important features of the resulting Φ statistics are captured for the case $h = 0$, which is simpler to analyze than finite h so $h = 0$ is considered. For this case, the PDF of χ is defined to be the continuum limit of the histogram of Φ^2 values immediately before mixing events.

The probability of $n > 0$ displacements between successive mixing events is $P(n) = 2^{-n}$. The Φ value is $n_+ - n_-$, denoting positive and negative steps respectively. In the large- n limit, random walk theory gives

$$P(\Phi|n) = \sqrt{\frac{2}{\pi n}} \exp\left(-\frac{\Phi^2}{2n}\right).$$

Now treating Φ and χ as continuous variables and recognizing that both positive and negative Φ contribute to given $\chi = \Phi^2$, the appropriate change of variables is applied to obtain

$$P(\chi|n) = \sqrt{\frac{2}{\pi n \chi}} \exp\left(-\frac{\chi}{2n}\right),$$

$$P(\chi) = \sum_{n=0}^{\infty} P(\chi|n)P(n) \approx \sqrt{\frac{2}{\pi \chi}} \int_0^{\infty} 2^{-n-(1/2)} \exp\left(-\frac{\chi}{2n}\right) dn.$$

For large χ , the Laplace method gives the leading-order χ dependence $P(\chi) \propto \chi^{-1/2} \exp[-(2\chi \ln 2)^{1/2}]$. This is a simple demonstration of the origin of the stretched exponential times $\chi^{-1/2}$, showing how randomly sampled instantaneous displacement and mixing events in a geometrically minimal setting can capture nontrivial features of turbulent scalar transport and mixing.

The analysis is conceptually analogous to a Lagrangian path integral in that the appropriately weighted average over all Lagrangian histories is evaluated, albeit lacking the local and global conservation constraints that a treatment based on fluid mechanics would impose. HiPS incorporates an internally consistent abstraction of those constraints, possibly accounting for the accuracy of the HiPS value of the stretch exponent.

The derived functional form of the large- χ PDF tail is likewise obtained for finite h , albeit through more complicated analysis. h might serve as a useful parameterization of, e.g., Sh dependence, possibly broadening the physical interpretation of figure 6.

REFERENCES

- BATCHELOR, G. K. 1959 Small-scale variation of convected quantities like temperature in a turbulent fluid. Part 1. General discussion and the case of small conductivity. *J. Fluid Mech.* **5**, 113–133.
- BOS, W. T. J. 2014 On the anisotropy of the turbulent passive scalar in the presence of a mean scalar gradient. *J. Fluid Mech.* **744**, 38–64.
- BRIARD, A. & GOMEZ, T. 2017 Prandtl number effects in decaying homogeneous isotropic turbulence with a mean scalar gradient. *J. Turbul.* **18**, 418–442.
- CHASNOV, J. 1991 Simulation of the inertial-conductive subrange. *Phys. Fluids A* **3**, 1164–1168.
- CHASNOV, J. & ROGALLO, R.S. 1988 Turbulence spectrum of a passive temperature field: Results of a numerical simulation. *Phys. Fluids* **31**, 2065–2067.
- CHERTKOV, M., FALKOVICH, G. & KOLOKOLOV, I. 1998 Intermittent dissipation of a passive scalar in turbulence. *Phys. Rev. Lett.* **80**, 2121–2124.
- CRAWFORD, F. W., HO, L. S. T. & SUCHARD, M. A. 2018 Computational methods for birth-death processes. *Wiley Interdisciplinary Reviews: Computational Statistics* **10**, e1423.
- CURL, R. L. 1963 Dispersed phase mixing: I. Theory and effects in simple reactors. *AIChE J.* **9**, 175–181.
- DONZIS, D. A., SREENIVASAN, K. R. & YEUNG, P. K. 2010 The Batchelor spectrum for mixing of passive scalars in isotropic turbulence. *Flow Turbul. Combust.* **85**, 549–566.
- ELSINGA, G., ISHIHARA, T. & HUNT, J. 2022 Non-local dispersion and the reassessment of Richardson’s t^3 -scaling law. *J. Fluid Mech.* **932**, A17.
- FOX, RODNEY O. 2003 *Computational Models for Turbulent Reacting Flows*. Cambridge University Press.
- GIRIMAJI, S.S. & POPE, S.B. 1990 Material-element deformation in isotropic turbulence. *J. Fluid Mech.* **220**, 427–458.

- GOTOH, T. & WATANABE, T. 2012 Scalar flux in a mean scalar gradient in homogeneous isotropic steady turbulence. *Physica D* **241**, 141–148.
- GOTOH, T. & YEUNG, P.K. 2013 Passive scalar transport in turbulence: a computational perspective. In *Ten Chapters in Turbulence* (ed. P.A. Davidson, Y. Kaneda & K. Sreenivasan), pp. 87–131. Cambridge.
- GURVICH, A. S. & YAGLOM, A. M. 1967 Breakdown of eddies and probability distributions for small-scale turbulence. *Phys. Fluids* **10**, 59–65.
- HILL, H.J. 1978 Models of the scalar spectrum for turbulent advection. *J. Fluid Mech.* **88**, 541–562.
- HOLZER, M. & SIGGIA, E.D. 1994 Turbulent mixing of a passive scalar. *Phys. Fluids* **6**, 1820–1837.
- KALDA, J. & MOROZENKO, A. 2008 Turbulent mixing: The roots of intermittency. *New J. Phys.* **10**, 093003.
- KERSTEIN, A. R. 1991a Scaling properties of the viscous-convective scalar spectral subrange in turbulent jets. *Phys. Fluids A* **3**, 1832–1834.
- KERSTEIN, A. R. 1991b Linear-eddy modelling of turbulent transport. Part 6. Microstructure of diffusive scalar mixing fields. *J. Fluid Mech.* **231**, 361–394.
- KERSTEIN, A. R. 2013 Hierarchical parcel-swapping representation of turbulent mixing. Part 1. Formulation and scaling properties. *J. Stat. Phys.* **153**, 142–161.
- KERSTEIN, A. R. 2014 Hierarchical parcel-swapping representation of turbulent mixing. Part 2. Application to channel flow. *J. Fluid Mech.* **750**, 421–463.
- KERSTEIN, A. R. 2021 Hierarchical parcel-swapping representation of turbulent mixing. Part 3. Origins of correlation patterns observed in turbulent boundary layers. *Phys. Rev. Fluids* **6**, 044611.
- KERSTEIN, A. R. 2022 Reduced numerical modeling of turbulent flow with fully resolved time advancement. Part 1. Theory and physical interpretation. *Fluids* **7**, 76.
- KOLMOGOROV, A. N. 1962 A refinement of previous hypotheses concerning the local structure of turbulence in a viscous in-compressible fluid at high Reynolds number. *J. Fluid Mech.* **13**, 82–85.
- KRAICHNAN, R.H. 1959 The structure of isotropic turbulence at very high Reynolds number. *J. Fluid Mech.* **5**, 497–543.
- KRAICHNAN, R.H. 1962 Turbulent thermal convection at arbitrary Prandtl number. *Phys. Fluids* **5**, 1374–1389.
- KRAICHNAN, R.H. 1974 Convection of a passive scalar by a quasi-uniform random straining field. *J. Fluid Mech.* **64**, 737–762.
- LIGNELL, D. O., FREDLINE, G. C. & LEWIS, A. D. 2015 Comparison of one-dimensional turbulence and direct numerical simulations of soot formation and transport in a nonpremixed ethylene jet flame. *Proc. Combust. Inst.* **35**, 1199–1206.
- LUNDGREN, T.S. 1981 Turbulent pair dispersion and scalar diffusion. *J. Fluid Mech.* **111**, 27–57.
- OBUKHOV, A. M. 1941 Spectral energy distribution in turbulent flow. *Izvestiya Akademii Nauk: SSSR. Seriya Matematicheskaya* **5**, 453–566.
- OBUKHOV, A. M. 1962 Some specific features of atmospheric turbulence. *J. Fluid Mech.* **13**, 77–81.
- O’GORMAN, P.A. & PULLIN, D.I. 2005 Effect of Schmidt number on the velocity-scalar cospectrum in isotropic turbulence with a mean scalar gradient. *J. Fluid Mech.* **532**, 111–140.
- POPE, S. B. 2000 *Turbulent Flows*. Cambridge University Press.
- RICHARDSON, L. 1926 Atmospheric diffusion shown on a distance-neighbour graph. *Proc. R. Soc. London, Ser. A* **110**, 709–737.
- SALAZAR, J.P.L.C. & COLLINS, L.R. 2009 Two-particle dispersion in isotropic turbulent flows. *Annu. Rev. Fluid Mech.* **41**, 405–432.
- SCATAMACCHIA, R., BIFERALE, L. & TOSCHI, F. 2012 Extreme events in the dispersion of two neighboring particles under the influence of fluid turbulence. *Phys. Rev. Lett.* **45**, 14501.
- SHETE, K.P., BOUCHER, D.J., RILEY, J.J. & DE BRUYN KOPS, S.M. 2022 Effect of viscous-convective subrange on passive scalar statistics at high Reynolds number. *Phys. Rev. Fluids* **7**, 024601.
- SHRAIMAN, B.I. & SIGGIA, E.D. 2000 Scalar turbulence. *Nature* **405**, 639–646.

- SU, L. K. & CLEMENS, N. T. 2003 The structure of fine-scale scalar mixing in gas-phase planar turbulent jets. *J. Fluid Mech.* **488**, 1–29.
- SUBRAMANIAM, S. & POPE, S. B. 1998 A mixing model for turbulent reactive flows based on Euclidean minimum spanning trees. *Combust. Flame* **115**, 487–514.
- TOUCHETTE, H. 2009 The large deviation approach to statistical mechanics. *Phys. Rep.* **478**, 1–69.
- WARHAFT, Z. 2000 Passive scalars in turbulent flows. *Annual Review of Fluid Mechanics* **32**, 203–240.
- WATANABE, T. & GOTOH, T. 2004 Statistics of a passive scalar in homogeneous turbulence. *New J. Phys.* **6**, 40.
- YEUNG, P. K. & SREENIVASAN, K. R. 2013 Spectrum of passive scalars of high molecular diffusivity in turbulent mixing. *J. Fluid Mech.* **716**, R14.
- YEUNG, P. K. & SREENIVASAN, K. R. 2014 Direct numerical simulation of turbulent mixing at very low Schmidt number with a uniform mean gradient. *Phys. Fluids* **26**, 015107.